

Dust Processing in Disks around T Tauri Stars

B. Sargent¹, W.J. Forrest¹, P. D'Alessio², A. Li³, J. Najita⁴, D.M. Watson¹, N. Calvet⁵, E. Furlan⁶, J.D. Green¹, K.H. Kim¹, G.C. Sloan⁶, C.H. Chen^{4,7}, L. Hartmann⁵, and J.R. Houck⁶

ABSTRACT

The 8–14 μm emission spectra of 12 T Tauri stars in the Taurus/Auriga dark clouds and in the TW Hydrae association obtained with the Infrared Spectrograph (IRS¹) on board *Spitzer* are analyzed. Assuming the 10 μm features originate from silicate grains in the optically thin surface layers of T Tauri disks, the 8–14 μm dust emissivity for each object is derived from its Spitzer spectrum. The emissivities are fit with the opacities of laboratory analogs of cosmic dust. The fits include small nonspherical grains of amorphous silicates (pyroxene and olivine), crystalline silicates (forsterite and pyroxene), and quartz, together with large fluffy amorphous silicate grains. A wide range in the fraction of crystalline silicate grains as well as large silicate grains among these stars are found. The dust in the transitional-disk objects CoKu Tau/4, GM Aur, and DM Tau has the simplest form of silicates, with almost no hint of crystalline components and modest amounts of large grains. This indicates that the dust grains in these objects have been modified little from their origin in the interstellar medium. Other

¹Department of Physics and Astronomy, University of Rochester, Rochester, NY 14627; bsargent@astro.pas.rochester.edu

²Centro de Radioastronomía y Astrofísica, UNAM, Apartado Postal 3-72 (Xangari), 58089 Morelia, Michoacan, Mexico

³Department of Physics and Astronomy, University of Missouri, Columbia, MO 65211

⁴National Optical Astronomy Observatory, 950 North Cherry Avenue, Tucson, AZ 85719

⁵Department of Astronomy, University of Michigan, 500 Church Street, Ann Arbor, MI 48109

⁶Center for Radiophysics and Space Research, Cornell University, Ithaca, NY 14853

⁷Spitzer Fellow

¹The IRS is a collaborative venture between Cornell University and Ball Aerospace Corporation funded by NASA through the Jet Propulsion Laboratory and the Ames Research Center.

stars show various amounts of crystalline silicates, similar to the wide dispersion of the degree of crystallinity reported for Herbig Ae/Be stars of mass $< 2.5 M_{\odot}$. Late spectral type, low-mass stars can have significant fractions of crystalline silicate grains. Higher quartz mass fractions often accompany low amorphous olivine-to-amorphous pyroxene ratios. It is also found that lower contrast of the $10 \mu\text{m}$ feature accompanies greater crystallinity.

Subject headings: circumstellar matter, infrared: stars, stars: pre-main-sequence

1. Introduction

It has long been known that T Tauri stars (TTSs) emit infrared (IR) radiation in excess of their stellar photosphere (e.g., Mendoza 1966). Cohen (1973) speculated that silicate dust in orbit around these stars was responsible for this excess emission. With observations from the *Infrared Astronomical Satellite* (IRAS), it was shown that the 12–100 μm IR excess emission from these young stars could arise from dusty accretion disks (Rucinski 1985). Many different models for this disk emission have been proposed. Both Adams et al. (1987) and Kenyon & Hartmann (1995) construct disk models including both accretion and reprocessing of stellar radiation. In order to explain how disk reprocessing can be responsible for the IR excesses of most TTSs, Kenyon & Hartmann (1987, henceforth KH87) proposed that disks around TTSs are flared, in that the scale height of the disk increases more than linearly with the distance from the central star. A flared disk intercepts a larger solid angle of radiation emitted from the star than a flat or nonflared disk, leading to more reprocessing of starlight. KH87 suggest that the surface of such a flared disk would become hotter than the midplane due to radiative transfer effects. The disk material is optically thick to $\lambda \sim 1 \mu\text{m}$ stellar radiation, so the starlight is absorbed in the highest layers of the disk. At $\lambda \sim 10 \mu\text{m}$, characteristic of the reprocessed radiation from the top disk layers at $R \sim 1 \text{ AU}$ in the disk, the disk has less optical depth, and the reprocessed radiation diffuses into the interior parts of the disk and heats those regions. For the small accretion rates typical of TTS, the disk atmosphere heats to a higher temperature than the layers in the disk underneath, and the vertical temperature inversion produces silicate features in emission (Calvet et al. 1992).

Dorschner (2003) summarizes how, based on the IR spectroscopic observations of Gillett et al. (1968), it came to be established that the $10 \mu\text{m}$ emission (or absorption) feature, the broad emission (or absorption) feature from 8 to $13 \mu\text{m}$ seen in a number of astronomical objects, is due to the Si–O stretching modes in silicate grains. Spectrophotometric observations by Forrest & Soifer (1976) and Forrest et al. (1976) at wavelengths longer than $16 \mu\text{m}$ provided further support for the silicate hypothesis. They found an $18.5 \mu\text{m}$ peak

in the Trapezium emission and an $18.5\ \mu\text{m}$ maximum in the absorption from the BN-KL source; the pairing of the $18.5\ \mu\text{m}$ feature (the broad emission or absorption feature from 16 to $23\ \mu\text{m}$) with the $10\ \mu\text{m}$ features in the Trapezium and the BN-KL source confirmed the silicate hypothesis.

There have been many studies of the silicate features of TTSs, both ground-based (Cohen & Wittetborn 1985; Honda et al. 2003; Kessler-Silacci et al. 2005) and space-based (Natta et al. 2000; Kessler-Silacci et al. 2006). However, ground-based spectroscopic observations are limited by the Earth’s atmosphere at mid-IR wavelengths in both wavelength coverage and sensitivity. Space-based missions, such as the *Infrared Space Observatory* (ISO; Kessler et al. 1996) do not suffer these limitations. The *Spitzer Space Telescope* (Werner et al. 2004) offers greater sensitivity than previous space-based missions. Here we focus on studying the $10\ \mu\text{m}$ silicate features of TTSs with the Infrared Spectrograph (IRS; Houck et al. 2004) on board Spitzer.

It is generally believed that the disks and planetary systems of young stellar objects (YSOs) form from material from the ISM. *Spitzer* IRS spectra of objects with Class I spectral energy distributions (SEDs) (Watson et al. 2004), objects believed to be young protostars still surrounded by collapsing envelope material from their parent cloud of gas and dust, show smooth, featureless $10\ \mu\text{m}$ absorption profiles, indicating amorphous silicates. Forrest et al. (2004) presented the spectrum of CoKu Tau/4, a T Tauri star with a $5\text{--}30\ \mu\text{m}$ spectrum well modeled by D’Alessio et al. (2005) by an accretion disk nearly devoid of small dust grains within ~ 10 AU. Unlike the complex $10\ \mu\text{m}$ emission features of many Herbig Ae/Be stars indicative of thermally processed silicates (Bouwman et al. 2001; van Boekel et al. 2005), the $10\ \mu\text{m}$ emission feature of CoKu Tau/4 is smooth, relatively narrow, and featureless, as are the silicate absorption profiles of the ISM (e.g., Kemper et al. 2004) and Class I YSOs (Watson et al. 2004). Smooth, narrow, and featureless profiles indicate amorphous silicates. Other objects, such as FN Tau (Forrest et al. 2004), have significant crystallinity of silicate dust in their disks, evident in the structure in their $10\ \mu\text{m}$ emission features, and others still, such as GG Tau A, have larger grains as shown by the greater width of the $10\ \mu\text{m}$ emission feature.

In the following, we use optical constants and opacities of various materials to model the $10\ \mu\text{m}$ features of our objects. We model the dust emission of the six objects whose spectra are presented by Forrest et al. (2004), TW Hya and Hen 3-600 A by Uchida et al. (2004), V410 Anon 13 by Furlan et al. (2005a), and GM Aur and DM Tau by Calvet et al. (2005); we also present and model the $5\text{--}14\ \mu\text{m}$ spectrum of GG Tau B. Stellar properties for our TTS sample are given in Table 1. In §2, we describe our data reduction techniques. In §3, we detail how we derive and fit an emissivity for each object, and in §4 we describe

the fit to the derived emissivity of each object. We discuss our fits in §5 and summarize our findings in §6.

2. Data Reduction

2.1. Observations

The present 12 TTS were observed with the IRS on board *Spitzer* over three observing campaigns from 2004 January 4 to 2004 March 5. All objects were observed with both orders of the Short-Low (SL) module ($R \sim 60\text{--}120$; second order [SL2], $\Delta\lambda = 0.06 \mu\text{m}$ [5.2–7.5 μm]; first order [SL1], $\Delta\lambda = 0.12 \mu\text{m}$ [7.5–14 μm]). Fainter objects were observed with the Long-Low (LL) module ($R \sim 60\text{--}120$; second order [LL2], $\Delta\lambda = 0.17 \mu\text{m}$ [14–21.3 μm]; first order [LL1], $\Delta\lambda = 0.34 \mu\text{m}$ [19.5–38 μm]), while brighter objects were observed with the Short-High (SH; $R \sim 600$, 9.9–19.6 μm) and Long-High (LH; $R \sim 600$, 18.7–37.2 μm) modules (the LH spectra are not used here).

The brightest objects were observed in mapping mode, in which for one module one data collection event (DCE; sampling of spectral signal from target) was executed for each position of a 2×3 (spatial direction \times spectral direction) raster centered on the coordinates of the target. For details on how the 2×3 maps were obtained, see the description of spectral mapping mode by Watson et al. (2004). From mapping-mode observations, we derive our spectra from the two positions in the 2×3 map for which the flux levels in the raw extracted spectra are highest. All other objects were observed in staring mode, which always immediately followed single high-precision Pointing Calibration and Reference Sensor (PCRS) peak-up observations. For details on IRS staring mode operation and PCRS observations, see Houck et al. (2004). For staring mode, the expected flux density of the target determined the number of DCEs executed at one pointing of the telescope; for faint objects, multiple DCEs were obtained at one pointing of the telescope and averaged together.

From the position of each target’s point-spread function (PSF) in the cross-dispersion direction in the two-dimensional data, we conclude that mispointing in the cross-dispersion direction in SL in mapping mode and in staring mode is usually less than $0''.9$ (half a pixel). By comparing the absolute flux levels of the spectra obtained from each of the three positions in a 1×3 subsection (the three positions are colinear and offset from each other in the dispersion direction of the slit) of the 2×3 raster, the pointing of the telescope in the dispersion direction in mapping mode could be determined. The mapping mode dispersion direction mispointing is usually less than half a pixel in SL ($0''.9$). Pointing in the dispersion direction cannot be quantified very easily for staring mode observations because the telescope

is not moved in the dispersion direction in this mode. To account for mispointing in the cross-dispersion direction, we use data that has been divided by the flatfield from the S11 pipeline. Mispointing in the dispersion direction primarily causes small photometric error; this will not affect the emissivities derived here.

2.2. Extraction of Spectra

The spectra were reduced using the Spectral Modeling, Analysis, and Reduction Tool (SMART; Higdon et al. 2004). From basic calibrated data (BCD; flat-fielded, stray-light-corrected, dark-current-subtracted) S11.0.2 products from the *Spitzer* Science Center IRS data calibration pipeline, permanently bad (NaN) pixels were fixed in our two-dimensional spectral data. The corrected pixel value was a linear interpolation of the nonbad pixels of the set of four nearest neighboring pixels (up, down, left, and right of the pixel in question). Unresolved lines of [Ne II] and molecular hydrogen, seen in the spectra of other objects, provided the wavelength calibration; all spectra presented in this paper are wavelength-corrected, and these wavelengths are estimated to be accurate to $\pm 0.02 \mu\text{m}$. All DCEs taken at the same pointing of the telescope (same module/order/nod position) were averaged together. Because one order records the spectrum of sky $\sim 1'–3'$ away from the target whose spectrum is being recorded in the module’s other order, sky subtraction in low resolution spectra obtained in staring mode is accomplished by subtracting the average spectrum from one spectral order of a given module from that in which the spectrum is located in the same nod position of the other order of the same module. For FM Tau, the SSC pipeline introduced artifacts in the off-order images in SL2. In this case, we used the same-order, different-nod DCE to subtract the sky.

The low-resolution sky-subtracted spectra were then extracted using variable-width column extraction in order to account for the linear increase of size of the object’s PSF with wavelength. From shortest to longest wavelengths of each module, respectively, extraction region width varied from 3.2 to 4.9 pixels in SL2, 3.6 to 4.4 pixels in SL bonus order (a short fragment of first-order light from $7.5–8.4 \mu\text{m}$ recorded simultaneously with SL2), 2.7–5.4 pixels in SL1, 3.2–4.9 pixels in LL2, 3.8–4.3 pixels in LL bonus order (a short fragment of first-order light from 19.4 to $20.9 \mu\text{m}$ recorded simultaneously with LL2), and 2.5 to 5.5 pixels in LL1. For SH the sky is not subtracted, as the SH slit is only 5 pixels long, and no separate sky observations were acquired. The extraction region at each wavelength for SH was the entire 5 pixel long slit. Since the roughly square SH pixels are $\sim 2''.2$ wide and SL pixels are $\sim 1''.8$ wide, the SH extraction region covered more solid angle at every wavelength than SL, and as spectra from SH typically gave lower flux than SL over the wavelength range

of overlap of SH with SL ($\sim 10\text{--}14\ \mu\text{m}$), the sky levels for the SH observations are estimated to be much lower than the flux density of the point sources.

The spectra are calibrated using a relative spectral response function (RSRF), which gives flux density, F_ν , at each wavelength based on the signal detected at that wavelength. The RSRFs were derived by dividing the template spectrum of a calibrator star by the result of extraction of the calibrator’s spectrum in SMART for each nod of each order of each module. For both orders of SL and for both orders of LL, a spectral template of α Lacertae (A1 V; M. Cohen 2004, private communication) of higher spectral resolution than the templates described by Cohen et al. (2003) was used, and a spectral template for ξ Dra (K2 III) was used for SH (Cohen et al. 2003). As with the science targets, SH observations of the calibrator source ξ Dra were not sky-subtracted. The science target raw extractions were then multiplied by the RSRFs corresponding to the same nod, order, and module. Typically, good flux agreement at wavelength regions of order overlap within the same module was found. As the spectra obtained for a given source at the telescope’s two nod positions are independent measurements of the object’s spectrum, close agreement between the two nod positions was expected; this was the case for all sources except for FN Tau.

2.3. Remaining technical problems

FN Tau was observed in mapping mode, and from the extracted flux levels of all observations in the 2×3 mapping raster, we determined that the central 1×2 pair both suffer mispointing of differing amounts. The more mispointed DCE was mispointed in the dispersion direction by $0''.7$, while the less mispointed DCE was mispointed in this direction by $0''.3$; both DCEs were mispointed in the cross-dispersion direction by between $0''.5$ and $0''.7$. The effect of this differential mispointing shows up most prominently in the derived spectrum of the more mispointed observation of first order of SL; there is a mismatch of flux level of about 10% over the entire order compared to the flux level of the spectrum obtained from the less mispointed DCE. To correct for this, the first order of the spectrum from the more mispointed mapping position was multiplied by 1.1 to match the less mispointed position. Except for the first order of SL for FN Tau, the derived spectra are the mean at each order of each module of the spectra from the two independent nod or map positions. For the first order of SL for FN Tau, the reported spectrum is that from only the less mispointed map position. Error bars are derived for each of the spectra, and the error bar at a given wavelength is equal to half the difference between the flux (at that wavelength) from the two nod (or map) positions used to derive the mean spectrum. For SL first order of FN Tau, the spectrum from the less mispointed map position and the corrected spectrum (previously

described) from the more mispointed map position were used to derive its error bars. Any error bar with relative uncertainty $<1\%$ is attributed to the low number (2) of measurements at that wavelength, and that errorbar is set to 1% of the flux.

There are some mismatches in flux between SL and SH, and between SL and LL in the spectra. Comparing the SL spectra of nonvariable sources to available photometry, absolute spectrophotometric accuracy is estimated to be better than 10% in SL. Therefore, small mismatches in flux levels between SL, SH, and LL are corrected by scaling the entire longer wavelength module to match the flux in SL, as we trust the photometric levels of SL. SH was multiplied by factors between 1.04 and 1.11 to match SL; LL for CY Tau was multiplied by 0.95 to match its SL spectrum. In order to account for off-order leaks in the filters which define the orders of each of the modules, the ends of each order of every module are truncated to guarantee the spectral purity of our spectra. The spectra of all objects in the sample excluding GG Tau B have been previously published: CoKu Tau/4, FM Tau, IP Tau, GG Tau A, FN Tau, and CY Tau in Forrest et al. (2004); TW Hya and Hen 3-600 A in Uchida et al. (2004); V410 Anon 13 in Furlan et al. (2005a); and GM Aur and DM Tau in Calvet et al. (2005). For all previously published spectra except the two by Calvet et al. (2005), wavelengths from 8 to $14\mu\text{m}$ were too long by $0.05\mu\text{m}$; as described previously, this wavelength problem was corrected before further analysis. The correction has moved the $9.4\mu\text{m}$ feature in FN Tau noted by Forrest et al. (2004) closer to $9.3\mu\text{m}$. In Figure 1, the spectrum obtained of the GG Tau B binary system is shown; in §4 we discuss the origin of the IR excess for this pair.

3. Analysis

3.1. Correction for Extinction

For all of the objects in the sample except V410 Anon 13, no correction for extinction is applied, in order not to introduce artifacts of overcorrection for extinction. See Table 1 for the assumed visual extinction A_V for each of the objects in our sample. No extinction correction is applied for any object having A_V less than 1.4; this includes all objects in the sample except CoKu Tau/4, GG Tau A, and V410 Anon 13. As described by D’Alessio et al. (2005), optical spectra of CoKu Tau/4 indicate time-dependent reddening to the star. This suggests that the source of the extinction to CoKu Tau/4 may be local to the object. However, the precise time and space dependence of extinction to CoKu Tau/4 is unknown. For this reason, no extinction correction is applied for CoKu Tau/4. White et al. (1999) estimate A_V of ~ 3.2 toward GG Tau Ab (the GG Tau system is a hierarchical quadruple with the northern pair, GG Tau A, being binary and separated by $0''.25$ – this is described

in greater detail in §4), while $A_V \approx 0.72$ toward GG Tau Aa. Consequently, no extinction correction is applied for GG Tau A, as it is believed the less extinguished GG Tau Aa component dominates the IRS spectrum.

For V410 Anon 13, an extinction correction is applied, assuming $A_V \approx 5.8$ along with Furlan et al. (2005a). Furlan et al. present a disk model for this object to fit its IRS spectrum assuming an inclination $i = 70^\circ$. Because of the large implied disk inclination, at least part of the extinction to V410 Anon 13 could be due to dust in the flared disk atmosphere at large disk radii lying in the sightline from the star and inner disk regions to observer. Furlan et al. (2005a) also found that when i in the model is changed from 70° to 60° , the peak of the flux in the $10 \mu\text{m}$ feature increases by $\sim 20\%$. Because the emergent disk spectrum in the model greatly depends on its inclination i , the effect of extinction correction for this object is discussed in §4.12 when describing its dust model fit. Because dust in the outermost reaches of YSO disks is expected to be little altered from its origin in the ISM (see the discussion in §5 below), the composition of any dust providing local extinction is assumed to be approximately the same as that in the ISM between V410 Anon 13 and Earth.

In the ISM, the ratio of the visual extinction to the optical depth at the $9.7 \mu\text{m}$ peak of the silicate absorption feature ($A_V/\Delta\tau_{9.7}$) varies by as much as a factor of 2 to 3 (see Draine 2003). To convert from A_V to the $9.7 \mu\text{m}$ extinction, we take $A_V/\Delta\tau_{9.7} \approx 18$, typical for the local diffuse ISM (see Draine 2003). For simplicity, we assume that the composition of the material responsible for the extinction does not change over the sightline from the target to Earth.

3.2. Derivation of Emissivity

The spectral excess for each of the objects in the sample is interpreted as arising from a disk surrounding one or more central star(s) beginning in most cases at a few stellar radii away from the central star(s) and extending as far away as a few hundred AU. We call a disk a “transitional disk” if it is optically thick to mid-IR wavelengths over some range of radii and optically thin elsewhere. CoKu Tau/4 (D’Alessio et al. 2005), DM Tau (Calvet et al. 2005), GM Aur (Calvet et al. 2005), TW Hya (Calvet et al. 2002), and Hen 3-600 A (Uchida et al. 2004) have been shown to be transitional disks through spectral modeling. The spectrum of CoKu Tau/4 is photospheric at wavelengths shortward of $8 \mu\text{m}$ but has a large IR excess seen in its IRS spectrum longward of that wavelength; correspondingly, it has an optically thick disk at radii greater than 10 AU with less than ~ 0.0007 lunar masses of small silicate dust grains inside that radius (D’Alessio et al. 2005). DM Tau has an IRS spectrum similar to that of CoKu Tau/4 and is modeled similarly by Calvet et al. (2005),

but with the radius of transition between the optically thick disk and the (very) optically thin inner regions at 3 AU. GM Aur, TW Hya, and Hen 3-600 A, also with large excess above photosphere longward of $8\ \mu\text{m}$, are not photospheric shortward of $8\ \mu\text{m}$. This excess indicates an optically thin inner disk region. The IR disk emission for each of the transitional disks is isolated by subtracting an appropriate stellar photosphere represented by a blackbody. For CoKu Tau/4 and DM Tau, the blackbody is fit to the 5–8 μm IRS spectral data, while for GM Aur, TW Hya, and Hen 3-600 A the Rayleigh-Jeans tail of the blackbody is fit to that of the stellar photosphere model by Calvet et al. (2005) and Uchida et al. (2004), respectively. This isolated disk emission for each object should, shortward of $\sim 20\ \mu\text{m}$, be due in large part to emission from the optically thin regions of the disk. For CoKu Tau/4 and DM Tau, this emission is mostly due to the optically thin regions of each object’s wall. For GM Aur, TW Hya, and Hen 3-600 A, this emission is mostly due to the optically thin inner disk regions (Calvet et al. 2005; Uchida et al. 2004).

We refer to a “full disk” if the disk is optically thick to mid-IR wavelengths throughout and extends from the dust-sublimation radius from the central star. Following the reasoning of Forrest et al. (2004), FM Tau, IP Tau, GG Tau A, GG Tau B, FN Tau, V410 Anon 13, and CY Tau are identified as having full disks based on their 5–8 μm spectra. Each has a continuum from 5 to 8 μm characterized by a spectral slope shallower than the Rayleigh-Jeans tail from a naked stellar photosphere. In addition, the 5 to 8 μm flux exceeds that from stellar photosphere alone (modeled by fitting a stellar blackbody to the near-IR photometry) by factors >2 . Following the discussion by Forrest et al. (2004), most of the 5–8 μm emission from full disks originates from optically thick inner disk regions, while most of the emission in the dust features above the continuum longward of $8\ \mu\text{m}$ is due to emission from dust suspended in the optically thin disk atmosphere. Therefore, a power law continuum is fit to the $<8\ \mu\text{m}$ region of each “full-disk” spectrum and subtracted from the spectrum to isolate the optically thin disk atmospheric emission.

Dust grains suspended in the optically thin atmosphere of a flared disk are directly exposed to stellar radiation, which heats the grains above the temperature of the disk’s photosphere. The grains then reemit the absorbed energy according to their temperature; this emission gives rise to the distinctive dust features seen in the spectra beyond $8\ \mu\text{m}$. The emission features are much narrower than a Planck function, which indicates structure in the dust emissivity. As explained in Calvet et al. (1992), a radiatively heated disk with a modest accretion rate has a thermal inversion. The upper layers of the disk, the optically thin disk atmosphere, are hotter than the lower layers, which are optically thick. This gives rise to spectral emission features characteristic of the dust in the disk atmosphere.

In modeling the SEDs of Classical T Tauri Stars (CTTSs), both Calvet et al. (1992) and

D’Alessio et al. (2001) compute the temperature of the atmosphere of each annulus of disk material as a function of vertical optical depth. In such models, it is assumed that all dust grains at a given height in an annulus are at the same temperature, independent of grain composition and grain size. It is similarly assumed here that all grains in any sufficiently small volume in a disk are at the same temperature, independent of grain composition and grain size. We aim for a simple model in order to determine the composition of the part of the disk giving rise to the optically thin dust emission. Bouwman et al. (2001) and van Boekel et al. (2005) also model dust emission by assuming a single temperature for all dust components. Optically thin emission from dust over the range of radii (and therefore temperatures) that contributes most to the 8–20 μm range is represented by emission from optically thin dust at a single, “average” temperature, T . It is assumed that the monochromatic flux of this optically thin emission over the short range from 8 to 14 μm is given by

$$F_\nu = \Omega_d \tau_\nu B_\nu(T) = \epsilon_\nu B_\nu(T) , \quad (1)$$

where F_ν is either the photosphere-subtracted residuals (for transitional disks) or power-law-continuum-subtracted residuals (for full disks); ϵ_ν is referred to as the emissivity; Ω_d is the solid angle of the region of optically thin emission; and τ_ν is the frequency-dependent optical depth of dust. For all objects except GG Tau B and GM Aur, T is found by assuming a long-to short-wavelength emissivity ratio, ϵ_l/ϵ_s , with “ l ” meaning long wavelengths ($\sim 20 \mu\text{m}$) and “ s ” meaning short wavelengths ($\sim 10 \mu\text{m}$), for dust and solving for T in the equation

$$\frac{F_\nu(\lambda_l)}{F_\nu(\lambda_s)} = \frac{\epsilon(\lambda_l)B_\nu(\lambda_l, T)}{\epsilon(\lambda_s)B_\nu(\lambda_s, T)} . \quad (2)$$

For GG Tau B, where no long-wavelength data exist, a dust temperature of 252 K is assumed, the same temperature as for GG Tau A. For reasons discussed in §4.4, the dust temperature is set to $T = 310$ K for GM Aur. For all other objects observed with SL and LL excluding DM Tau, we take the 20 μm -10 μm flux ratios; for the objects observed in SL, SH, and LH, we decrease the wavelengths in the ratio to 19.3 and 9.65 μm , as SH does not extend to 20.0 μm . In a single-temperature dust model, the same temperature will be computed regardless of the wavelengths used to determine the flux ratio due to the properties of the Planck function. The wavelengths were set to 9.5 and 19.0 μm for DM Tau as a test to determine if the derived temperature depended much on the exact choice of wavelengths used to determine flux ratio. When the wavelengths were changed to 10 and 20 μm for DM Tau, the computed temperature changed from 160 to 158 K; however, this did not require any change to the DM Tau dust model. A similar test was performed on FN Tau by changing the long and short wavelength fluxes used for its dust temperature determination from 10 and 20 μm to 9.5 and 19 μm . This increased dust temperature from 208 to 209 K; as with DM Tau, no change to the FN Tau dust model was required.

Using this temperature, T , the photosphere- or continuum-subtracted residuals were divided by $B_\nu(T)$ to give the emissivity, which is proportional to the mass-weighted sum of opacities as follows:

$$\epsilon(\lambda) \propto \sum_j m_j \kappa_j(\lambda) = \sigma(\lambda) \quad , \quad (3)$$

where m_j is the mass fraction of dust component j , $\kappa_j(\lambda)$ is the wavelength-dependent opacity ($\text{cm}^2 \text{g}^{-1}$) of dust component j , and $\sigma(\lambda)$ is the wavelength-dependent cross-section of the dust mixture model. Both $\epsilon(\lambda)$ and $\sigma(\lambda)$ are normalized to unity at their peak in the 8–14 μm range.

To determine the uncertainties in the emissivities, the corresponding spectral error bars, obtained as described in §2.3 from spectra obtained at two nod positions, are divided by $B_\nu(T)$, the result of which is then divided by the same normalization constant used to derive the corresponding emissivity. The derived emissivities are believed to be valid immediately longward of 8 μm , where the 10 μm feature rises above the extrapolation of the $< 8 \mu\text{m}$ continuum, as no drastic change of the slope of the continuum from the optically thick components of the disks at wavelengths between 8 and 14 μm is expected. However, assuming one dust temperature for a wide range of wavelengths in a spectrum of a circumstellar disk is unrealistic. In addition, for wavelengths longward of $\sim 14 \mu\text{m}$, the slope of the continuum from optically thick emission is not well determined by extrapolation from the $< 8 \mu\text{m}$ continuum. The power-law-continuum- or photosphere-subtracted residual flux at $\sim 20 \mu\text{m}$, attributed as described previously to optically thin emission, is therefore uncertain, leading to uncertainty in the derived dust temperature. For this reason, we do not attempt to fit the 18 μm and longer wavelength features here. The emissivity is fit by finding the optimal set of mass fractions, m_j , such that the normalized model dust cross-section fits the normalized emissivity as well as possible. The fitting method is iterated until the assumed ϵ_l/ϵ_s , used to compute grain temperature and therefore derive emissivity, equals the ϵ_l/ϵ_s derived from the fit emissivities; ϵ_l/ϵ_s and other details of derivation of emissivities are reported for each of the opacity models in Table 2. Also listed in Table 2 is $\beta_{9.9}$, the ratio of the continuum-subtracted residual flux at 9.9 μm to the 9.9 μm continuum of the full disks, which gives the contrast of the silicate emission feature to the optically thick continuum in the original spectrum.

3.3. Disk Model for IP Tau

As a test of these simple dust models, a disk model following the methods of D’Alessio et al. (1998, 1999, 2001) was computed, using stellar parameters from Table 1 and the mass accretion rate from Hartmann et al. (1998). First, opacities similar to those generated from

the fit to the emissivity of IP Tau (see §4.7) were used to determine the temperature structure of the disk, but it was found that the disk would not heat up sufficiently—the spectrum generated from this model had lower flux than the IP Tau spectrum at all wavelengths. A source of dust opacity with high absorption at visible and near-IR wavelengths was needed to absorb the stellar radiation and heat up the disk to give more flux at all IRS wavelengths (5–36 μm). Facing the same issue when attempting to model the interstellar extinction, Draine & Lee (1984) added in an artificial source of absorption for $\lambda < 8 \mu\text{m}$ in their “astronomical silicates” for similar reasons (also see Jones & Merrill 1976; Rogers et al. 1983). Therefore, the optical properties of graphite and “astronomical silicates” from Draine & Lee (1984) were used to determine the radial and vertical temperature structure of the disk. Then, opacities obtained from the fit to the IP Tau 10 μm feature were used to determine the emergent spectrum. This disk model uses the same dust opacities at all radii and at all heights in the disk. As can be seen in Figure 2, the 5–12 μm model spectrum is in quite good agreement with the observed spectrum of IP Tau. It is concluded that the emissivities derived here are basically correct. At wavelengths $> 12 \mu\text{m}$, the model gives more flux than is observed. There is too much emission from cool grains with respect to that from warm grains. This may be an indication that dust in the IP Tau disk is more settled (settling meaning that the dust-to-gas ratio in the disk atmosphere is lower than that at the disk midplane) than assumed in the model. According to D’Alessio et al. (2006) and Furlan et al. (2005b), more settling of dust reduces disk emission at wavelengths $> 20 \mu\text{m}$ more than shortward of 20 μm .

3.4. Dust Components

The material in YSO circumstellar disks originates from the ISM. Draine & Lee (1984) fit the interstellar extinction with silicates and graphite; here, the spectra are also fit with opacities derived from silicates and carbonaceous material. Silicates, which contain SiO_x groups, give rise to 10 and 18 μm features from the bonds between Si and O. The 10 μm feature arises from Si–O stretching modes, while the 18 μm feature is due to O–Si–O bending modes. Crystalline silicate grains have many narrow, strong resonances, while amorphous silicate grains, lacking ordered structure, give rise to two broad, weaker resonances; one near 10 μm and one near 18 μm . From Dorschner et al. (1995), the optical constants for amorphous pyroxene of composition $\text{Mg}_{0.8}\text{Fe}_{0.2}\text{SiO}_3$ and amorphous olivine of composition MgFeSiO_4 are used. In this paper, these dust components are referred to as “amorphous pyroxene” and “amorphous olivine,” respectively; collectively, they are referred to as “amorphous silicates.” For optical constants of the three crystalline axes of forsterite of composition $\text{Mg}_{1.9}\text{Fe}_{0.1}\text{SiO}_4$, data from Fabian et al. (2001) is used. The same bulk density, 3.3 g cm^{-3} , is assumed for forsterite and all small amorphous olivine and pyroxene grains. This value is obtained from

Pollack et al. (1994) for the high end of the range of densities for “high-T silicate”. For large amorphous olivine and pyroxene grains, this value is the bulk density of the matrix for large porous amorphous olivine and pyroxene grains (see §3.5 for discussion on how porosity modifies the density of a grain). For crystalline pyroxene, mass absorption coefficients for $\text{Mg}_{0.9}\text{Fe}_{0.1}\text{SiO}_3$ (En90, having $\text{Mg}/(\text{Mg}+\text{Fe}) \sim 0.9$) by Chihara et al. (2002) are used. Chihara et al. report this crystalline pyroxene to have monoclinic structure. To represent the opacity profile of silica (SiO_2), the dispersion parameters for the ordinary ray and extraordinary ray of α quartz by Wenrich & Christensen (1996) are used. The density of α quartz assumed is 2.21 g cm^{-3} , which is the value for amorphous silica stated by Fabian et al. (2000). This is also close to the values of 2.27 and 2.32 g cm^{-3} for tridymite and cristobalite (polymorphs of silica), respectively (Etchepare et al. 1978). Such a value for the density of quartz is chosen because it is deemed likely (see discussion in §4) that forms of silica other than α quartz are present in the disks studied here, possibly in greater mass fractions than α quartz. The nominal value for α quartz is 2.65 g cm^{-3} , as is given in Etchepare et al. (1978). Because opacity is inversely proportional to density, and because the density of quartz is potentially underestimated here, the silica profile may need to be multiplied by a constant slightly less than 1; therefore, our mass fractions for quartz could be underestimated by as much as a factor of $(2.21/2.65) \sim 0.83$. For the T Tauri sample in this paper, we find that adequate fits to the dust emissivity do not require large crystalline silicate grains.

As articulated by Dorschner et al. (1995), glassy amorphous silicates produced and analyzed in laboratories on Earth are too “clean”, meaning that they do not give enough opacity in the $13\text{--}16 \mu\text{m}$ trough between the 10 and $18 \mu\text{m}$ silicate features to account for the dust emissivities of Mira variable stars. Clean silicates also have too little absorption shortward of $8 \mu\text{m}$; Jones & Merrill (1976) and Rogers et al. (1983) argued that circumstellar silicates must be “dirty” to account sufficiently for the absorption of stellar radiation by dust in shells around evolved stars. The derived disk emissivities in our study of T Tauri stars also require a relatively featureless source of continuum opacity longward of $13 \mu\text{m}$. The source of this continuum opacity is not well constrained because it has no distinctive spectral features. We use amorphous carbon to supply the continuum opacity, as carbonaceous material is believed to be a major component of the ISM (e.g., Draine & Lee 1984; Li & Greenberg 1997). Zubko et al. (1996) argue in favor of amorphous carbon as a major component of interstellar and circumstellar dust, and Bradley (2003) asserts that a large fraction of the carbon found in chondritic interplanetary dust particles (IDPs) is amorphous. For amorphous carbon, the optical constants for the “ACAR” mixture (Zubko et al. 1996) are used, and a bulk density for amorphous carbon grains of 2.5 g cm^{-3} (Lisse et al. 1998) is assumed.

3.5. Dust Shape and Size

In addition to grain composition, grain shape and grain size affect the computed dust opacities. The presence of interstellar polarization indicates that interstellar grains must be both elongated and aligned (Draine 2003). Dyck et al. (1973) observed in the Becklin-Neugebauer (BN) source in Orion a correlation of the linear polarization with the optical depth of the $10\ \mu\text{m}$ silicate band, leading them to propose the existence of nonspherical aligned silicate grains in front of BN. For an approximation of actual grain shapes, we assume here a CDE2 shape distribution (Fabian et al. 2001) for small amorphous silicates and amorphous carbon dust in our models. In CDE2, all ellipsoidal shapes are included, but the distribution is peaked toward near-spherical shapes, and extreme shapes such as needles or flat sheets are given zero weight. CDE2 requires all grains to be in the Rayleigh limit ($2\pi a/\lambda \ll 1$, where a is the radius or characteristic size of grain). This condition is generally met by submicron-sized grains for the IRS wavelengths ($\lambda > 5\ \mu\text{m}$). For the shape distributions of quartz and forsterite, the continuous distribution of ellipsoids (CDEs; Bohren & Huffman 1983) is used, in which all shapes are equally weighted, because this shape distribution fits the observed dust features in the emissivities better than the CDE2 shape distribution. We note in the Appendix that $0.1\ \mu\text{m}$ sized porous grains of α quartz and forsterite give rise to opacity profiles nearly identical to those of solid grains of α quartz and forsterite with the CDE distribution, respectively. We do not suggest that the small crystalline grains are porous, but we note this identity. For forsterite, it is assumed that the three crystalline axes are randomly oriented with respect to the three ellipsoidal axes. As with CDE2, CDE also assumes particles much smaller than the wavelengths of interest. Because opacities for crystalline pyroxene grains ground in an agate mortar (Chihara et al. 2002) are used, no definitive statements about the grain shape distribution for this species of dust can be made. As described by Sogawa et al. (1999), forsterite was ground into powder; when observed with a scanning electron microscope, the forsterite particles constituting the powder are observed to be nonspherical. The only statement that can be made about these particles' sizes is that they are submicron (Sogawa et al. 1999). The same is assumed to be true for the crystalline pyroxene grains described by Chihara et al. (2002).

Grain growth is accounted for by including opacities derived from grains of a single size to represent large grains, following Bouwman et al. (2001) and van Boekel et al. (2005); see those references for descriptions of the sizes and shapes of the grains they used. Mie theory (Bohren & Huffman 1983) can be used to obtain exact results for the opacity of solid spherical grains of arbitrary size; however, large grains grown by coagulation in protoplanetary disks are expected to have an irregular and porous structure (see Li & Lunine 2003 and references therein). To account for this heterogeneity of large grains, the Bruggeman effective medium theory (EMT; Bohren & Huffman 1983) is used, following Li & Lunine (2003), in deriving

the effective dielectric functions of large fluffy grains. Lisse et al. (1998) found that using these effective dielectric functions in Mie theory could approximate the absorption efficiency of grains with fractal dimension D , a measure of the porosity (volume fraction of empty space) in a given grain, between 2.5 and 3; $D=3$ for solid grains, while $D < 3$ represents porous grains. The effective dielectric functions computed from the Bruggeman EMT are used in Mie theory to derive the absorption efficiencies of spherical porous grains. Harker et al. (2002) use the EMT with $2.5 < D < 3$ to model the fluffy grains in comet Hale-Bopp (also see Li & Greenberg 1998; Lisse et al. 1998). The optical depth through the center of the grains is preserved, in order to match the opacity profile of the solid $2 \mu\text{m}$ amorphous silicate grains used by Bouwman et al. (2001). Optical depth (τ_λ) and bulk silicate opacity (κ_λ) are kept the same for both solid and porous grains, assuming the silicate matrix of a porous grain has the same opacity as that of an equivalent-mass solid grain, and the diameter for the porous grain is obtained by $\tau_\lambda = \rho \kappa_\lambda d$, where ρ is the mass density of the grain [equal to the bulk silicate density (that of a solid silicate grain) times $(1 - f)$, where f is the volume fraction of vacuum]. For $f = 0.6$, a porous grain of radius $5 \mu\text{m}$ has the same optical depth as that through a solid $2 \mu\text{m}$ radius sphere. The fractal dimension was chosen to be 2.766, a number which is within the acceptable range for D . The 8–14 μm opacity profile of these porous grains with radii $a = 5 \mu\text{m}$, $D = 2.766$ and $f = 0.6$ (i.e. 60% of their volume is vacuum) is very similar to that of solid spherical ($f = 0$, $D = 3$) amorphous silicate grains of radii $\approx 2 \mu\text{m}$. In this paper, by “large grains” we mean porous amorphous olivine or pyroxene grains of radii $a = 5 \mu\text{m}$, volume fraction of vacuum $f = 0.6$, and dimension $D = 2.766$.

3.6. Degeneracy among Dust Component Opacities

Our fits to the disk emissivities are not necessarily unique. The degeneracy in the mass fraction of amorphous silicate components is larger than for crystalline silicate components. For instance, much of the broad, smooth opacity profile of either of the large silicate grain components overlaps with both that of the other large silicate grain component and both of the small amorphous silicate opacity profiles. There is less uncertainty associated with the two small amorphous silicate profiles, as they are narrower and stronger than the profiles of the large amorphous silicates. There is even less uncertainty regarding the crystalline silicate components, as their profiles are even narrower and often stronger than any of the amorphous silicate profiles. Some crystalline silicate identifications may be confused by overlapping bands: the opacity profile of crystalline pyroxene has a peak at $\sim 9.3 \mu\text{m}$ that is close in wavelength to the $9.2 \mu\text{m}$ feature of quartz; the prominent $\sim 11.3 \mu\text{m}$ peak of forsterite is very close to the weak $11.2 \mu\text{m}$ feature of crystalline pyroxene. In addition, there are polymorphs and forms of silica other than α quartz (see §3.4). Speck (1998) gives 7.5–

13.5 μm extinction profiles for silica; they all peak at around 9.1–9.2 μm . This implies a very large degeneracy between the different polymorphs and forms of silica. In addition, there is degeneracy between different forms and polymorphs of crystalline pyroxene. The extinction efficiency of clinopyroxene from Koike et al. (1993) shows a 9.3 μm peak higher than the other two major peaks in the 10 μm region. If one takes the Chihara et al. (2002) profile of crystalline pyroxene (En90, which is monoclinic) and adds silica, boosting the 9.3 μm feature, and also forsterite, boosting the crystalline pyroxene features between 11 and 12 μm , one obtains a profile with feature strengths similar to that reported for clinopyroxene in Koike et al. (1993). Therefore, there is degeneracy between clinopyroxene and a mixture of silica, forsterite, and the crystalline pyroxene used here (En90). The featureless opacity continuum from amorphous carbon may be reproduced by silicate grains larger than $\sim 20 \mu\text{m}$ in radius, which give essentially featureless continuum for 8–20 μm wavelengths.

4. Results

The 10 μm emissivity profiles of the ISM, μ Cep, and three of our transitional disks are compared in Figure 3, as described in §4.1 and Table 3. In Figures 4, 5, and 6 the derived emissivities and model fits are shown for the 12 T Tauri stars. The parameters of the model fits are detailed in Table 4.

4.1. Comparison between ISM, μ Cep, and Transitional Disks

Figure 3 compares the smoothest, simplest 10 μm silicate emission features in the TTS sample to the derived optical depth profile of the interstellar absorption towards GCS 3 in the Galactic center from Kemper et al. (2004, Fig. 3b) and the 10 μm feature of μ Cep (Sloan et al. 2003), a mass-losing M2 Ia supergiant (Forrest et al. 1979). According to Levesque et al. (2005), the visual extinction A_V for μ Cep is ~ 2 , so no correction for extinction is applied. For μ Cep, the emissivity was derived by first subtracting a model photosphere of $T_{eff} = 3500 \text{ K}$, $\log(g) = 0$, and solar metallicity by Brott & Hauschildt (2005), binned to the *ISO* Short Wavelength Spectrometer (SWS) spectral resolution. Following the procedure outlined in §3.2, a silicate temperature of 423 K was derived, based on the residuals at 10 and 18.2 μm . The GCS 3 profile from Kemper et al. (2004) is displayed unaltered. In order to compare the TTS and μ Cep profiles with the GCS 3 profile, a first-order baseline was fit to each of the emissivities at ~ 8 and $\sim 13 \mu\text{m}$ and subtracted from the corresponding emissivity; each residual is scaled to the peak of the GCS 3 profile. The parameters used for this process are listed in Table 3. All five silicate profiles in Figure 3 are generally smooth.

The profiles of TTS peak at wavelengths closer to the peak of the ISM profile than to that of μ Cep, which peaks at a somewhat longer wavelength. The close similarity between the GCS 3 ISM profile and the TTS profiles strongly supports the assertion that the dust in YSO disks comes from the ISM.

4.2. CoKu Tau/4

The smoothest, least complex T Tauri $10\ \mu\text{m}$ feature is that of CoKu Tau/4. D’Alessio et al. (2005) model this object as a standard flared disk of modest inclination with nearly all small grains in the inner 10 AU cleared: literally, a disk in transition. This modeling indicates less than 0.0007 lunar masses of grains of ISM grain size ($< 0.25\ \mu\text{m}$) remain in the inner disk. This configuration is remarkable considering the estimated age of the CoKu Tau/4 system, which is only 1–3 Myr. The $10\ \mu\text{m}$ silicate feature in this model is dominated by emission from the cylindrical disk “wall” at the 10 AU truncation radius. The outer layers of this wall are roughly isothermal, as each point on the wall is ~ 10 AU from the star; as such, the emissivity for CoKu Tau/4, derived by assuming all grains are at a single temperature, is a reasonable first approximation. The derived dust temperature for CoKu Tau/4 is ~ 121 K, which is well within the range of temperatures in Figure 4 of D’Alessio et al. (2005) computed using amorphous pyroxene and amorphous olivine grains in the optically thin region of the CoKu Tau/4 wall. This temperature alone indicates the bulk of the material is located ~ 10 AU from the star as noted by Forrest et al. (2004).

The $10\ \mu\text{m}$ silicate profile of CoKu Tau/4 is quite similar to that of the ISM (see Figure 3). A satisfactory fit (Figure 4) is achieved with nonspherical small amorphous pyroxene and olivine grains with a mass ratio of 3.73:1. Kemper et al. (2004) fit the $10\ \mu\text{m}$ interstellar silicate absorption profile toward the Galactic center source GCS 3 with small spherical amorphous pyroxene and olivine grains with a mass ratio of 0.18:1. Most of this difference in mass ratio comes from the differing adopted shape assumptions. The CDE2 grain shape distribution assumed here shifts the $9.8\ \mu\text{m}$ peak from spherical amorphous olivine grains to $9.95\ \mu\text{m}$ and the $9.3\ \mu\text{m}$ peak from spherical amorphous pyroxene grains to $9.4\ \mu\text{m}$. In addition, the CoKu Tau/4 profile peaks at a slightly shorter wavelength ($9.55\ \mu\text{m}$) than the GCS 3 ISM profile ($9.6\ \mu\text{m}$). This could indicate a slight compositional difference, although note the large error bars for $\lambda < 9.55\ \mu\text{m}$ in CoKu Tau/4. The lack of narrow features on top of the amorphous feature indicates negligible amounts of crystalline grains. At 1–3 Myr, the dust from 10 AU outward in the CoKu Tau/4 disk shows little evidence for processing.

Although small nonspherical grains of amorphous olivine and pyroxene account successfully for the peaks of the 10 and $18\ \mu\text{m}$ features, the model with small silicate grains does not

account for a very small excess of emissivity on the long-wavelength side of the CoKu Tau/4 $10\ \mu\text{m}$ feature. Optically thick emission from the dust would widen the $10\ \mu\text{m}$ feature, but it would do so to both the long- and short-wavelength sides of the feature. Larger amorphous silicate grains, however, can account for this $11.5\text{--}12.5\ \mu\text{m}$ excess. Larger grains (see §3) give greater opacity longward of the $10\ \mu\text{m}$ silicate peak, but not shortward. Consequently, porous silicate grains of $5\ \mu\text{m}$ radius are included 4.3% by mass in the CoKu Tau/4 dust model.

While models consisting of only silicates can account for the positions and shapes of the 10 and $18\ \mu\text{m}$ features, the $12\text{--}15\ \mu\text{m}$ opacity continuum from laboratory silicates is lower than that in the derived CoKu Tau/4 emissivity. Amorphous carbon is used to model this excess continuum opacity (§3).

4.3. DM Tau

DM Tau is also a disk in transition. At disk radii interior to 3 AU, less than 0.0007 lunar masses of submicron-sized grains remain (similar to CoKu Tau/4), according to Calvet et al. (2005). The derived dust temperature for DM Tau, 160 K, is only slightly higher than that for CoKu Tau/4 (121 K), which reinforces the conclusion that DM Tau has no inner dust disk (see §4.2). As with CoKu Tau/4, the disk at radii larger than 3 AU is optically thick, and the spectrum from 5 to $8\ \mu\text{m}$ is photospheric. The $10\ \mu\text{m}$ feature is of somewhat low contrast to the underlying photosphere, but our derived emissivity is well fit with small grains of amorphous olivine and pyroxene, large $5\ \mu\text{m}$ porous amorphous olivine grains, and amorphous carbon. No crystalline grains are indicated by the DM Tau profile (Figure 4).

4.4. GM Aur

Calvet et al. (2005) assert that GM Aur is also a transition disk, albeit with a slightly more complex radial distribution of dust than for CoKu Tau/4 or DM Tau. Their model includes an optically thin inner disk from the dust sublimation radius out to 5 AU containing ~ 0.02 lunar masses of small dust grains, negligible small dust grains between 5 and 24 AU, and a full outer disk beyond 24 AU. The usual method of computing dust temperature self-consistently based on the short- to long-wavelength flux ratio derived from the photosphere-subtracted residuals results in a very poor fit to the derived GM Aur emissivity. That method gives $T \sim 210\ \text{K}$, with 50% by mass small amorphous pyroxene, 33% small amorphous olivine, and 17% amorphous carbon, resulting in a χ^2 per degree of freedom (dof)

of ~ 100 , severely underestimating the emissivity for $\lambda < 9 \mu\text{m}$ and slightly overestimating the emissivity longward of $13 \mu\text{m}$. Therefore, a self-consistent dust temperature of $T = 386 \text{ K}$ was determined for GM Aur using the fluxes at 9.4 and $18.8 \mu\text{m}$ of the optically thin inner disk component from the GM Aur model of Calvet et al. (2005). This gave a somewhat better fit to the computed emissivity. The model required $\sim 53\%$ by mass small amorphous olivine and $\sim 47\%$ amorphous carbon and gave a χ^2/dof of 44.4 , with the dust model overestimating the emissivity shortward of the $10 \mu\text{m}$ feature peak and underestimating the emissivity longward of $12.5 \mu\text{m}$.

The low dust temperature of 210 K resulted from including emission from the very cold wall at 24 AU in the model of Calvet et al. (2005). The second method excludes the wall emission and gave a dust temperature of 386 K . The dust model assuming dust at 210 K underestimates the $8 \mu\text{m}$ emissivity while the model assuming 386 K dust overestimates the $8 \mu\text{m}$ emissivity (and the opposite effects happen at $\sim 14 \mu\text{m}$). Therefore, the dust temperature is set between 210 and 386 K to achieve the optimal fit to the derived emissivity. By setting $T = 310 \text{ K}$, a χ^2/dof of ~ 9.8 was achieved using the dust mass fractions listed in Table 4, adequately fitting the computed $8\text{--}14 \mu\text{m}$ emissivity. Amorphous olivine is included to match the $\sim 9.8 \mu\text{m}$ central wavelength of the GM Aur $10 \mu\text{m}$ feature. Amorphous pyroxene and amorphous carbon are also included; however, no large amorphous silicate grains are indicated, as any amount of such grains would make the model $10 \mu\text{m}$ feature wider than that observed. Likewise, the spectrum indicates negligible amounts of crystalline silicates and quartz.

4.5. TW Hya

TW Hya is another suspected transitional disk (Calvet et al. 2002; Uchida et al. 2004). Calvet et al. (2002) propose that it is a disk partially cleared out to $\sim 4 \text{ AU}$; gas and ~ 0.5 lunar masses of grains of radii $\sim 1 \mu\text{m}$ populate the inner optically thin disk. Uchida et al. (2004) found a transition radius of 3.3 AU instead of 4 AU based on the IRS spectrum of TW Hya. The outer disk is assumed to be optically thick. The derived dust temperature for TW Hya, 193 K , is low (as with CoKu Tau/4) compared to the dust temperatures of other stars in our sample, which further supports TW Hya relatively lacking inner disk material. The $10 \mu\text{m}$ feature of TW Hya is smooth, like those of CoKu Tau/4 and DM Tau; little crystalline material is indicated. The derived emissivity peaks at $9.55 \mu\text{m}$, indicating a high-mass fraction of amorphous pyroxene. A fairly substantial large grain content is indicated, $\sim 24.5\%$ by mass. Approximately 1% by mass of forsterite is indicated by the slight knee at $11.3 \mu\text{m}$. TW Hya shows two small peaks at 12.4 and $12.8 \mu\text{m}$. According to Speck (1998),

various forms of amorphous and crystalline silica have features peaking between 12 and 13 μm . Quartz is the only one with two peaks at roughly 12.4 and 12.8 μm . This indicates $\sim 1\%$ quartz by mass. At wavelengths shorter than 8.7 μm , however, the emissivity rises above the model. The data in Speck (1998) shows that other forms of silica may better fit this short-wavelength “shoulder.” We intend to investigate this in a future study using a larger sample of TTS spectra.

With an age of ~ 10 Myr (Webb et al. 1999; Weintraub et al. 2000), TW Hya has very little crystalline material, which is somewhat unexpected. A number of the disks in Taurus from our sample, which like CoKu Tau/4 are believed to be 1–3 Myr old, have significantly greater crystalline mass fractions than TW Hya. Hen 3-600 A, another system in the TW Hydrae association, has much greater mass fractions of crystalline grains, making it an interesting counterpoint. This issue is discussed further in §5.

4.6. FM Tau

FM Tau has a slightly more complex 10 μm feature than the Taurus transitional disks. The 5–8 μm continuum for this object is shallower than, and well in excess of, the stellar photosphere, implying that the optically thick disk around this object extends inward to the dust sublimation radius (Forrest et al. 2004). The 10 μm feature of FM Tau peaking around 9.6–9.7 μm is narrow. It is fit with negligible amounts of large grains. Forrest et al. (2004) note that the spectrum of this object has a “knee” at 11.3 μm , indicating the presence of forsterite. The mass fraction of forsterite used in the dust opacity model for FM Tau is only $\sim 0.3\%$. The model spectrum is higher than the emissivity at < 8.3 μm . This is attributed to uncertainty in the subtraction of the power law (which was fit to the optically thick emission immediately shortward of 8 μm), as the derived emissivity immediately longward of 8 μm is more sensitive to the absolute level of the power law than the emissivity at longer wavelengths.

4.7. IP Tau

IP Tau is similar to FM Tau. Forrest et al. (2004) also ascribe a full disk extending to the dust sublimation radius for this object. The 10 μm feature peaks at ~ 9.6 –9.7 μm and is only slightly wider than that of FM Tau, indicating large amorphous olivine grains of $\sim 7\%$ by mass. The 11.3 μm knee of IP Tau is more prominent than that of FM Tau, indicating a higher crystalline mass fraction of forsterite (2%) than for FM Tau.

The opacities used to fit the emissivity of IP Tau are very similar to those used in the IP Tau disk model described in §3.3; there are exceptions. Instead of using CDE2 as the shape distribution for small amorphous olivine and amorphous pyroxene, the CDE shape distribution was used. For the same reasons that the assumed shape distribution affected the ratio of amorphous pyroxene to amorphous olivine for GCS 3 and CoKu Tau/4 (see discussion in §4.2), the use of CDE instead of CDE2 for the small amorphous silicates slightly increased the amorphous pyroxene to amorphous olivine ratio. Also, 2 μm radius solid grains of amorphous olivine were used instead of 5 μm radius porous amorphous olivine grains; however, as noted before, the opacity profile of 5 μm porous amorphous silicate grains is nearly identical to that of 2 μm solid amorphous silicate grains. In addition, graphite was used in place of amorphous carbon to give opacity continuum.

4.8. GG Tau A

GG Tau A has the next most complex 10 μm feature. GG Tau A is binary, and White et al. (1999) estimate masses from Baraffe et al. (1998) stellar evolutionary models of $0.78 \pm 0.10 M_{\odot}$ for Aa and $0.68 \pm 0.03 M_{\odot}$ for Ab. The separation of the two is $0''.25$ (~ 35 AU). Our spectrum is the sum of GG Tau Aa and GG Tau Ab. Similar to FM Tau and IP Tau, the 5–8 μm continuum from GG Tau A is well in excess of the stellar photospheres, which led Forrest et al. (2004) to conclude that there is a full inner disk in GG Tau A. The circumbinary dust disk outside of 35 AU from the center of mass of the GG Tau A pair would be too cold to give rise to the 10 μm emission seen from GG Tau A. Grains of composition of “astronomical silicates” from Draine & Lee (1984) at 252 K in radiative equilibrium with a blackbody of radius $2 R_{\odot}$ and $T_{\text{eff}} = 4000$ K (representing the radiation from one star of the GG Tau A pair) would be located ~ 1 AU from the star. The dust temperature of 252 K (Table 2) implies that silicate grains are located ~ 1 AU from either Aa or Ab (or both). This is consistent with the finding by Najita et al. (2003) of CO emission originating less than 2 AU from one (or both) of the two stars of the GG Tau A system. Following Simon & Prato (1995), regarding disk partitioning in multiple systems, it is assumed that the IR excess must originate from a circumstellar disk around Aa or Ab, or both. White et al. (1999) report $\text{H}\alpha$ emission of 57 Å equivalent width (EW) from Aa but only 16 Å EW from Ab, suggesting a more substantial inner disk around the Aa component. However, this disk must be truncated outward of a few AU, otherwise the interactions with the Ab component would disrupt a larger disk. The emissivity peaks at 9.5 μm , indicating large amounts of amorphous pyroxene. Mass fractions of large silicate grains similar to TW Hya are indicated, definitely higher than those for FM Tau and IP Tau. A prominent 11.3 μm feature indicates a forsterite mass fraction similar to that for IP Tau. Quartz is suggested by possible features at 12.4

and $12.8\ \mu\text{m}$.

4.9. GG Tau B

The IRS mapping-mode observation of GG Tau A also included signal from GG Tau B in the SL slit. GG Tau B is about $10''$ due south of GG Tau A, and it is also a binary (White et al. 1999). The position angle of the SL slit for each position of the GG Tau A map was $\sim 344^\circ$, close to the position angle of the separation of GG Tau A and GG Tau B, so GG Tau A and B were close to maximally separated in the Short-Low slits of two of the map positions. The spectrum of GG Tau B was extracted from the two map positions best centered on its position. The Short-Low slit is 2 pixels ($3''.6$) wide, and the extraction aperture used varies from as little as 3.3 pixels ($6''$) at the shortest wavelength of first order to as much as 5 pixels ($9''$) at the longest wavelength. This extraction region was centered on GG Tau B; at the longest wavelengths, the edge of the extraction region in SL closest to GG Tau A is ~ 2 – 3 pixels away from the center of the PSF of GG Tau A, which is believed to be sufficiently far away to minimize contribution of signal from GG Tau A. White et al. (1999) report the two components of the GG Tau B binary, Ba and Bb, to be separated by $1''.48$ (207 AU), which is smaller than the Short-Low beam. The spectrum shown for GG Tau B therefore includes signal from both Ba and Bb, as well as from circumstellar disk(s) around either or both stars. White et al. (1999) assign masses of $0.12 \pm 0.02 M_\odot$ for Ba and $0.044 \pm 0.006 M_\odot$ for Bb, and report $\text{H}\alpha$ EW of $\sim 20\ \text{\AA}$ for Ba and 20 – $43\ \text{\AA}$ for Bb. This puts both Ba and Bb near the hydrogen-burning mass limit. The $10\ \mu\text{m}$ feature from the GG Tau B pair indicates a higher mass fraction of crystalline grains than any of CoKu Tau/4, TW Hya, FM Tau, IP Tau, or GG Tau A. Because the $10\ \mu\text{m}$ emission from GG Tau B is seen and also because the separation between Ba and Bb is ~ 200 AU, it is believed that a circumstellar disk(s) exist(s) around either Ba or Bb, or both. It is unclear to which component, Ba or Bb (or both), the GG Tau B disk emission belongs. Currently, we have no long-wavelength data for GG Tau B, so instead of deriving a silicate dust temperature for GG Tau B, the same dust temperature for GG Tau A, 252 K, is used. The peak of the $10\ \mu\text{m}$ feature is much flatter than that of any of the previous sources, with sharp inflections at 9.4 and $11.2\ \mu\text{m}$ defining the plateau. Due to the low signal (~ 80 mJy at $10\ \mu\text{m}$), the S/N is rather low, so only a rough fit to the $10\ \mu\text{m}$ feature was attempted. The narrow peak in emissivity at $\sim 9.4\ \mu\text{m}$ suggests crystalline pyroxene. The plateau shape of the rest of the $10\ \mu\text{m}$ feature is due to larger grains and an admixture of small crystalline grains of other composition—*forsterite*, in this model.

The emissivity and dust model deviate longward of $12.5\ \mu\text{m}$. Noting that the flux at

SL wavelengths for GG Tau A is roughly 10 times that for GG Tau B, and noting that the extraction aperture is largest for the longest wavelengths of the first order of SL, we attribute the $>12.5 \mu\text{m}$ rise of emissivity above model to contamination of signal from GG Tau A.

4.10. Hen 3-600 A

Hen 3-600 is another multiple system with mid-IR emission. Jayawardhana et al. (1999) resolve the Hen 3-600 system into A and B components and measure a separation of components of $1''.4$ (70 AU assuming the Hen 3-600 pair belongs to the TW Hydrae association). In addition, Hen 3-600 A itself is a spectroscopic binary (Torres et al. 2003). None of the components of the Hen 3-600 system are resolved in any of the instrument slits (Uchida et al. 2004), but Jayawardhana et al. (1999) determined that the circumstellar disk is associated with the A pair. Due to the unknown separation of components of the spectroscopic binary, the disk(s) in this system cannot be assigned to either of the components. It is assumed that the A pair are separated by less than 1 AU and that the IRS spectrum for Hen 3-600 A arises from a circumbinary disk around the A pair. The combined luminosity of the two components from Webb et al. (1999) are listed in Table 1. Honda et al. (2003) and Uchida et al. (2004) report that the $10 \mu\text{m}$ feature for this object indicates amounts of crystalline silicates comparable to those of amorphous silicates.

The derived dust temperature for Hen 3-600 A is $\sim 229 \text{ K}$, higher than for other transitional disks. This means that this object has more grains in its inner disk than other transitional disks, consistent with a transition radius of 1.3 AU (Uchida et al. (2004)), the closest (to the star) among all transitional disks. The $10 \mu\text{m}$ feature (Figure 6) shows a $9\text{--}11 \mu\text{m}$ plateau, along with a strong, narrow feature at $9.2 \mu\text{m}$. The $9.2 \mu\text{m}$ feature indicates quartz in the CDE distribution (Wenrich & Christensen 1996; Speck 1998). Silica was previously identified by Uchida et al. (2004) and Honda et al. (2003). Alpha quartz produces smaller peaks at 12.4 and $12.8 \mu\text{m}$, which may correspond to a small feature centered at $12.6 \mu\text{m}$ in the emissivity. Alternatively, other polymorphs and forms of silica give single-peaked features at $\sim 12.6 \mu\text{m}$ (Speck 1998), so it is quite possible that other forms or polymorphs of silica may be present in Hen 3-600 A. In addition to quartz, a larger mass fraction of the material responsible for the continuum opacity than for any other objects in this sample is needed to fit the $12\text{--}14 \mu\text{m}$ continuum. Small amorphous carbon grains are assumed, but it could just as well come from very large silicate grains. The overall flatness of the $10 \mu\text{m}$ plateau indicates a small amount of crystalline pyroxene. Forsterite is indicated by the sharp $11.3 \mu\text{m}$ edge of the plateau, and small and large grains of amorphous pyroxene are added to smooth the crystalline silicate features between 9.2 and $11.3 \mu\text{m}$. The emissivity

rises above the dust model from 13 to 14 μm , although much less drastically than for GG Tau B. Such a feature in the emissivity could be due to a dust component other than what we use for Hen 3-600 A.

4.11. FN Tau

The derived emissivity of FN Tau also indicates a large crystalline silicate mass fraction. The plateau top to the 10 μm feature is not flat, but it slopes downward to longer wavelengths, more so than for Hen 3-600 A. The derived emissivity of FN Tau peaks at 9.3 μm , a bit longer than that of Hen 3-600 A. It also has minor peaks at 9.9, 10.6, 11.2, and 11.5 μm . All of these peak positions are highly indicative of crystalline pyroxene. Amorphous pyroxene smooths the narrow subfeatures at the top of the 10 μm sloping plateau, while simultaneously accentuating the 9.3 μm feature. Approximately 1% by mass of quartz is indicated by the model. Like TW Hya, there is a “shoulder” at wavelengths shorter than 8.7 μm that may indicate a silica type other than α quartz. Like GG Tau B and Hen 3-600 A, the dust model underestimates the emissivity at wavelengths near 14 μm (see the discussion of GG Tau B).

4.12. V410 Anon 13

The V410 Anon 13 emissivity is similar to those of FN Tau and Hen 3-600A. V410 Anon 13 is a very low-mass star ($\sim 0.1 M_{\odot}$; Furlan et al. 2005a) of spectral type M5.75; quite remarkably, it is surrounded by a full, flared accretion disk. Like FN Tau, the derived emissivity peaks at 9.3 μm , indicating crystalline pyroxene as opposed to quartz. No clear identification can be made for any features (or lack thereof) between 12 and 13 μm due to relatively high spectral noise, so a small amount of quartz is not ruled out. Like Hen 3-600 A, the rest of the 10 μm feature is a fairly featureless flat plateau with a sharp knee at 11.2 μm . The sharp 11.2 μm knee indicates forsterite. Small grains of amorphous pyroxene emphasize the 9.3 μm feature and dampen the crystalline features of forsterite and crystalline pyroxene along the top of the 10 μm plateau. As with FN Tau, the 8.7 μm shoulder and the emissivity between 13 and 14 μm are both underestimated by the dust model.

Because the extinction correction was only applied for V410 Anon 13, the effects of changing the extinction correction on the dust model for this object were explored. As discussed previously, it is believed that any local extinction would be very similar to the interstellar extinction, so only the amount of extinction was varied. When the optical depth of intervening material was doubled (from $\tau_{9.7} = 0.32$ to $\tau_{9.7} = 0.64$), the derived dust tem-

perature increased from 256 to 289 K. The inferred mass fraction of amorphous pyroxene increased from 48% to 61%, quartz decreased from 2% to 1%, crystalline pyroxene decreased from 11% to 10%, forsterite decreased from 5% to 2%, and amorphous carbon decreased from 34% to 26%. The χ^2/dof increased slightly from 1.9 to 2.1, but the fit still looked reasonable. The increase of derived dust temperature results from the opacity of interstellar silicates being higher in the $10\ \mu\text{m}$ feature than in the $20\ \mu\text{m}$ feature. The modest increase in the mass of amorphous pyroxene is attributed to the variation of the amount of extinction correction over the $10\ \mu\text{m}$ feature. The extinction correction is greatest near $\sim 9.7\ \mu\text{m}$, vertically “stretching” the $10\ \mu\text{m}$ feature so that more amorphous pyroxene, peaking at $9.4\ \mu\text{m}$, is needed. The extinction correction also has the effect of “rounding off” any narrow peaks due to crystalline silicates, such as the $11.3\ \mu\text{m}$ peak best fit by forsterite, thus decreasing the amount of crystalline silicates. In addition, this stretching raises the contrast of the $10\ \mu\text{m}$ feature above the $>13\ \mu\text{m}$ continuum, effectively decreasing the amount of continuum opacity required from amorphous carbon.

4.13. CY Tau

The most troublesome emissivity to characterize was that of CY Tau. While the $5\text{--}8\ \mu\text{m}$ excess of this object is similar to those of the other full disks in our sample, the contrast of the $10\ \mu\text{m}$ excess to the underlying continuum is the lowest in the entire sample (very low $\beta_{9.9}$; see Table 2). For this reason, the derived emissivity is poorly determined over the entire $10\ \mu\text{m}$ feature. What can be discerned is a fairly narrow feature around $9.3\ \mu\text{m}$ (as with FN Tau and V410 Anon 13), and a noisy downward slope to $\sim 11.4\ \mu\text{m}$, at which point the feature sharply drops. While large grains can provide flat-topped $10\ \mu\text{m}$ features of low contrast, they cannot produce the $9.3\ \mu\text{m}$ opacity sharp peak; therefore, only a modest amount of large grains are included. Between the local minima at 11.8 and $13.2\ \mu\text{m}$ in the emissivity, a small feature rises above the pixel-to-pixel noise, followed by a rise past $13.5\ \mu\text{m}$ to longer wavelengths. Crystalline pyroxene can account for the $9.3\ \mu\text{m}$ peak, while the $11.4\ \mu\text{m}$ inflection indicates forsterite. As with V410 Anon 13, quartz is consistent within the noise near $12.5\ \mu\text{m}$. In addition, quartz provides, as with Hen 3-600A, a boost to the crystalline pyroxene at $9.3\ \mu\text{m}$ to increase its prominence, while at the same time giving rise to spectral features in the 12 to $13\ \mu\text{m}$ region accounting for some of the noisy features between 11.8 and $13.2\ \mu\text{m}$. Amorphous pyroxene is included to provide overall roundness to the $10\ \mu\text{m}$ feature. As with FN Tau, the dust model underestimates the derived CY Tau emissivity near $14\ \mu\text{m}$.

5. Discussion

5.1. Lack of Processing of Silicates in Transitional Disks

Li & Draine (2001) conclude that no more than 5% of the Si in the diffuse ISM is in crystalline silicates. Kemper et al. (2004) place an upper limit of $\sim 2.2\%$ for the silicate dust toward the Galactic center. The result of $\sim 0.1\%$ mass fraction of crystalline silicates (forsterite, crystalline pyroxene, and quartz) for CoKu Tau/4 and nearly zero crystalline silicates for DM Tau and GM Aur (Table 4), is therefore consistent with nearly no processing of silicate dust in these disks, and with the material in these disks having originated from the ISM. This seems to indicate that little processing occurs in the outer disks, or, if processing does occur in the inner disk, the dust in the inner disk is not transported efficiently to the outer disk. Perhaps the material in the inner optically thin disk of GM Aur was located between 10 and 24 AU immediately before the planet formed near 24 AU. This material would have experienced no processing, as in the case of CoKu Tau/4. Perhaps a planet opened up a disk gap at ~ 24 AU, halting inward accretion at 24 AU of material from the outer disk. The disk inside of 24 AU would continue accreting, and perhaps the last of this inner disk of nonprocessed dust is seen just before it gets accreted onto the star. In Figure 7 the mass fraction of crystalline silicates $M_{\text{cryst.sil}}/M_{\text{sil}}$ versus wall radius is plotted for the five transitional disks. Note the lack of crystallinity for disks with walls beyond 2 AU.

5.2. Comparison of T Tauri Stars to Herbig Ae/Be Stars

The spectra of the rest of the 1–3 Myr old Taurus sample, all of which have inner disks more substantial than those of CoKu Tau/4, DM Tau, and GM Aur, indicate that crystalline silicates constitute at least $\sim 0.5\%$ (by mass) of all silicates in each disk. Whatever is responsible for producing the crystalline grains in T Tauri disks therefore appears linked to the inner 3 AU disk region, a finding in line with the spectrointerferometric observations of Herbig Ae/Be disks (van Boekel et al. 2004). A substantial crystalline component is in place in the “full” T Tauri disks (defined in §3.2) at 1–3 Myr. In our sample of TTSs, a majority of the silicate dust mass is always found in amorphous silicates.

The disks in the sample with lower mass fractions of crystalline silicates indicate forsterite but no crystalline pyroxene, while the disks with higher crystalline silicate mass fractions indicate both types of crystalline silicates. This is consistent with the trend reported by van Boekel et al. (2005) regarding the disks around Herbig Ae stars. Confirming this trend will require a larger sample and a more thorough investigation of the degeneracy between forsterite and crystalline pyroxene (see discussion in §3.6).

All spectra except V410 Anon 13 indicate some large grains, but a greater crystalline mass fraction does not appear to correlate with a greater large-grain mass fraction (see Figure 8) for the T Tauri objects in our sample. See the discussion in §3.5 on how grain sizes and shapes assumed in this study compare to those in other studies (Bouwman et al. 2001; van Boekel et al. 2005). Because quartz accounts for less than $\sim 3\%$ of the total dust mass in the models, this implies that the mass fraction of forsterite and crystalline pyroxene does not correlate with that of the $5\ \mu\text{m}$ sized porous amorphous silicate grains. It seems reasonable that, over time, the mass fraction of crystalline grains would increase, as should the mass fraction of large grains in disks around stars. However, crystallization and grain growth are not the same processes—crystallization involves changing the grain structure at the atomic level, while grain growth involves the gradual clumping together of small grains to aggregate into large grains. The rates of increase of the crystalline grain mass fraction and of the large grain mass fraction should not necessarily be the same for even one single YSO disk. Furthermore, silicate grain growth and crystallization of silicate dust might proceed at different rates in disks with different accretion rates, mass, etc. It is not clear why large-grain mass fraction and crystalline grain mass fraction should be correlated in Herbig Ae/Be stars (van Boekel et al. 2005) but not in T Tauri stars.

It is also curious that V410 Anon 13 indicates a substantial mass fraction of crystalline silicates but a negligible mass fraction of large grains. If, as proposed by Weidenschilling (1997), large grains in disks settle more quickly than smaller grains toward the optically thick midplane, and vertical convection is negligible (as is expected due to the vertical temperature inversion in disk atmospheres), then the lack of larger grains in a disk may simply be due to the fact that large grains have settled from the optically thin atmosphere of the disk, where they can be seen, down to the optically thick midplane. A high mass fraction of very large grains could be present in the V410 Anon 13 disk atmosphere and only produce a featureless continuum.

Van Boekel et al. (2005) report that Herbig Ae/Be stars of mass greater than $2.5 M_{\odot}$ have consistently high mass fractions of crystalline silicates ($\sim 20\%$ to $\sim 30\%$), and that Herbig Ae/Be stars less massive than $2.5 M_{\odot}$ have crystalline silicate mass fractions varying widely between 0 and $\sim 20\%$. It is found that, like the lower mass Herbig Ae/Be stars, TTSs of mass $\sim 1.2 M_{\odot}$ down to $\sim 0.1 M_{\odot}$ exhibit large dispersions in the mass fractions of crystalline silicates. Silicates in the disks around the lowest mass stars in our sample—FN Tau, V410 Anon 13, GG Tau B—have the highest crystalline percentages (between $\sim 27\%$ and $\sim 30\%$) in our sample. According to the mass tracks from several different stellar evolutionary models, FN Tau (spectral type M5; Kenyon & Hartmann 1995) is less massive, ($\sim 0.28 M_{\odot}$; Siess et al. 2000) than all other stars in our sample except V410 Anon 13 and the component stars of the GG Tau B pair. The disks in our sample with the highest mass fractions of

crystalline silicates surround the lowest mass stars. A study of silicate crystallinity as a function of stellar mass for a much larger sample is underway (D. M. Watson et al. 2006, in preparation). The mass fraction of crystalline silicates $M_{\text{cryst.sil}}/M_{\text{sil}}$ versus stellar mass is plotted in Figure 9. Using the mass fraction of only forsterite and crystalline pyroxene instead of $M_{\text{cryst.sil}}$ in Figure 9 would not greatly change it as quartz is never a major component of the total crystalline grain mass. The emissivities of Hen 3-600 A and GG Tau B (both known as binary systems), indicate some of the highest mass fractions of crystalline grains in our sample; the emissivity of the binary GG Tau A (which is coeval with GG Tau B, according to White et al. (1999)), however, indicates a low mass fraction of crystalline silicates.

5.3. Production of Crystalline Silicate Dust

Numerous mechanisms have been proposed for processing amorphous silicate grains into crystalline silicates. Based on the MIDI (Mid-IR Interferometric Instrument) spectra, van Boekel et al. (2004) argue that in the inner disk regions (<2 AU), crystalline silicate grains are condensed directly from the gas phase. Alternatively, solid amorphous silicates may be thermally annealed into crystalline grains; in thermal annealing, grains are heated sufficiently that constituent atoms redistribute themselves in the grain in more energetically favored positions, forming a regular crystalline lattice (Brucato et al. 1999). Various mechanisms have been proposed to transport grains radially from the warm inner disk regions, where crystalline silicates may be produced, to the outer disk regions. These include convection and turbulent mixing (Boss 2004), turbulent diffusion and large-scale circulation currents (Gail 2004), and X -winds (Shu et al. 1996).

Spectra of CoKu Tau/4 and DM Tau indicate that almost no crystalline silicates exist in the regions emitting the mid-IR spectra. For CoKu Tau/4, this region is mostly the vertical wall at ~ 10 AU. For DM Tau, the region giving rise to much of its mid-IR spectrum is a combination of the wall at ~ 3 AU and the cooler optically thin atmosphere immediately beyond the wall (Calvet et al. 2005). The lack of crystalline silicate grains in the outer disks of these two objects (beyond ~ 3 AU for DM Tau and beyond ~ 10 AU for CoKu Tau/4) seems to suggest that very few crystalline silicate grains were radially transported to their outer disks; however, this may be expected in the case of planet formation and inner disk clearing. After a planet forms, it can clear out a gap in a disk, and any newly formed crystalline silicate dust interior to the planet’s orbit will either be accreted onto the planet or onto the star. Furthermore, crystalline dust in the upper layers of the outer disk will accrete inward onto the newly formed planet.

Local production of crystalline grains is an alternative to radial transport. Lightning

has been proposed (Pilipp et al. 1998) to heat dust grains and chondrules, but it is not clear exactly whether lightning in YSO disks might be generated (Desch & Connolly 2002). Harker & Desch (2002) propose *in situ* annealing at disk radii between ~ 5 and 10 AU, summarizing evidence that chondrules (which contain crystalline silicates) formed from circumstellar material in young disks between ~ 5 and 10 AU; therefore, they look to that region as the site of dust grain annealing. Harker & Desch (2002) propose that submicron- to micron-sized dust grains are heated and annealed by thermal exchange with surrounding gas, itself heated by a disk shock front; the rate of cooling of the grains is then determined by the rate of cooling of the surrounding disk gas. Their simulations, using models described by Desch & Connolly (2002), indicate that silicate grains can be annealed in 5 km s^{-1} shocks out to 10 AU. In some simulations, $250 \mu\text{m}$ radius chondrules were completely evaporated. According to Boss & Durisen (2005a), shock fronts have been seen in simulations of gravitationally unstable disks as transient phenomena. To initiate gravitational instability, Wood (1996) asserts that the ratio of the disk mass to the stellar mass must be around 0.3 to 0.5; however, in some numerical simulations, disk-to-star mass ratios as low as 0.05 (Boss & Durisen 2005b) initiate the growth of gravitational instability in a disk, resulting in the formation of a spiral arm. This spiral arm would then be the site of shock annealing.

In an attempt to characterize the degree of likelihood of such shock processing to occur, disk mass relative to stellar mass in our small sample is considered. It is not known to which component of the GG Tau A binary the GG Tau A disk emission belongs, so it is not included in our discussion of the effect of the ratio of the disk mass to the stellar mass on the mass fraction of crystalline grains; for the same reason, GG Tau B is not included. In addition, there are no disk mass estimates for V410 Anon 13 and Hen 3-600 A, so they are not included. In Figure 10 we plot the disk-to-star mass ratio versus the mass fraction of crystalline silicates. There is no clear correlation between the disk-to-star mass ratio and the silicate crystallinity. As with Figures 8 and 9, when quartz is excluded from the total crystalline mass fraction, the conclusion does not change (i.e. there is no correlation between the disk-to-star mass ratio and the total mass of crystalline pyroxene and forsterite).

It is possible that planet formation may obscure any correlation between the disk-to-star mass ratio and the crystalline silicate mass fraction. Gravitational instabilities may induce disk shocks. If planets form by gravitational instability, which should be correlated with the disk-to-star mass ratio, then planets should form when disk shocks are in the process of annealing silicate grains. Any crystalline silicates produced by disk shocks, which are interior to the forming planet, would then either accrete onto the planet or onto the star, thus eventually removing any evidence of them. The relation (or lack thereof) of the disk mass-to-star mass ratio with the crystalline mass fraction for a much larger sample of objects in the Taurus-Auriga star-forming region will be studied in a forthcoming paper.

In Figure 11 is plotted for the full disks the mass fraction of crystalline silicates versus $\beta_{9.9}$, the measure of the contrast of the $10\ \mu\text{m}$ feature to the underlying continuum. Note that the disks with lower crystallinity have higher $\beta_{9.9}$, and those with high degrees of crystallinity have lower $\beta_{9.9}$. The mass fraction of large silicate grains versus $\beta_{9.9}$ is plotted in Figure 12. Here an upper envelope, decreasing for increasing $\beta_{9.9}$, to the large grain fraction may be present. Others have observed in Herbig Ae/Be stars (van Boekel et al. 2003) and T Tauri stars (Przygodda et al. 2003; Kessler-Silacci et al. 2005, 2006) a trend of decreasing the $10\ \mu\text{m}$ feature contrast with increased dust processing (grain growth and/or dust crystallization). The decrease of both the crystallinity and the large grains mass fractions with increasing $\beta_{9.9}$ in our sample of 12 T Tauri disks is consistent with the earlier studies.

At 10 Myr, Hen 3-600 A presents a disk with a large mass fraction of crystalline silicates, while TW Hya does not. TW Hya ($\sim 0.7 M_{\odot}$; see Webb et al. 1999 and Siess et al. 2000) is hypothesized to have a protoplanetary or planetary companion orbiting between ~ 2 and 3 AU (Calvet et al. 2002) and is reported to have a fairly massive disk of $\sim 0.03 M_{\odot}$ (Wilner et al. 2000). Uchida et al. (2004) show that the optically thin disk inside of ~ 3.3 AU is responsible for most of the $10\ \mu\text{m}$ emission in TW Hya. While the spectrum of TW Hya does indicate a small amount of forsterite and quartz, and a substantial fraction of large grains, it does not indicate crystalline pyroxene; the derived crystalline mass fractions for TW Hya are similar to those of GG Tau A and IP Tau, but TW Hya is much older than those stars. Perhaps the protoplanetary companion to TW Hya orbiting at 2-3 AU prevents outward radial transfer of crystalline silicate grains produced in the inner disk; alternatively, perhaps the small star-planet separation allows only a small zone in which shocks can form, annealing fewer silicate grains. The transition from optically thin inner disk to optically thick outer disk is modeled to be at ~ 1.3 AU in Hen 3-600 A (Uchida et al. 2004), indicating a more substantial disk in Hen 3-600 A than in TW Hya. Hen 3-600 A is the only one transitional disk with a substantial degree of crystallinity (see Figure 7). The denser disk between 1.3 and 3.3 AU in Hen 3-600 A might lead to either more inner disk crystalline silicate production and freer radial transport of crystalline grains or more substantial shock processing than in TW Hya.

5.4. Possible Connection between Quartz and Amorphous Pyroxene

There is an indication of increasing mass fraction of quartz with decreasing mass fraction ratio of amorphous olivine to amorphous pyroxene (Figure 13). The IRS spectra of TW Hya, Hen 3-600 A, and GG Tau A all indicate the presence of quartz and low amorphous olivine to amorphous pyroxene mass ratios. We caution, however, that our sample size is small (12

spectra), and that further study of this possible trend, using a much larger sample of spectra, will be needed to verify this finding. Furthermore, some of the mass in quartz in these disks could be in forms of silica other than α quartz, which would affect this trend. These issues will be explored in a future paper.

6. Summary and Conclusions

The $10\ \mu\text{m}$ features in 10 TTS spectra from the Taurus-Auriga star-forming region and 2 spectra from the TW Hydrae Association are modeled by deriving the emissivities from IRS spectra of the optically thin dust emission. Through an iterative process of varying dust grain mass fractions of various dust species to match the dust cross-sections to the derived emissivities and using the derived $\sigma(\sim 20\ \mu\text{m})/\sigma(\sim 10\ \mu\text{m})$ ratios to recompute the dust temperature (and therefore self-consistently define the emissivity), the modeled emissivities are fit with a multi-component dust model.

To test the simple single-temperature approach of deriving and fitting the $10\ \mu\text{m}$ feature emissivities, a wavelength-dependent dust cross-section similar to the one generated from the fit to IP Tau was used to determine the emergent spectrum in a model of its emission, and it was found that the fit to the spectrum of IP Tau requires a significant source of absorption at visible/near-IR wavelengths. To fit the interstellar extinction, Draine & Lee (1984) also required a source of absorption at these wavelengths in addition to that from known silicates. Consequently, graphite and “astronomical silicates” were used to determine the radial and vertical temperature structure of the model disk for IP Tau, and a dust mixture similar to the best-fit dust mixture for this object was used to compute the emergent spectrum from the model disk. This full radiative transfer model gave an excellent fit to the $5\text{--}12\ \mu\text{m}$ spectrum of IP Tau, supporting the simplified emissivity modeling technique used here. The model predicts too much emission at wavelengths longer than $12\ \mu\text{m}$, indicating too much emission in the model from cooler dust grains, suggesting there is settling of dust from the disk atmosphere to the midplane.

Our 12 object sample indicates the following:

- Almost all the T Tauri disks show some degree of silicate crystallinity, irrespective of star mass or age.
- Transitional disks, disks whose inner portions are either partially or nearly totally cleared of small dust grains, usually indicate very few crystalline silicate grains.
- Theories of radial transport of crystalline silicates in T Tauri disks are constrained to explain the ISM-like lack of crystalline silicates outward of 3 AU in DM Tau and

outward of 10 AU in CoKu Tau/4, both of which are 1–3 Myr old systems.

- No obvious correlation of the mass fraction of crystalline silicate grains with that of large silicate grains exists for the T Tauri sample. This contrasts with the results of van Boekel et al. (2005) for Herbig Ae/Be systems (see discussion in §3.5 regarding differences in grain shape and size between this study and Bouwman et al. [2001] and van Boekel et al. [2005]).
- The 10 μm features always indicate a majority of mass in amorphous silicate grains.
- Crystalline pyroxene is usually accompanied by forsterite, but the reverse is not necessarily true.
- Very low mass stars can have relatively large amounts of crystalline silicates in their surrounding disks.
- No clear trend exists between the mass fraction of crystalline silicates and the disk-to-star mass ratio.
- For full disks, high contrast of the 10 μm feature, as measured by $\beta_{9.9}$, indicates both low crystallinity and small mass fraction of large grains; decreasing contrast of the 10 μm feature for these disks indicates increasing crystallinity and a range of mass fractions of large grains. This is consistent with studies of Herbig Ae/Be stars (van Boekel et al. 2003) and previous studies of T Tauri stars (Przygodda et al. 2003; Kessler-Silacci et al. 2005, 2006).
- There is an indication that higher quartz mass fraction accompanies lower amorphous olivine to amorphous pyroxene ratio.

One of the surprising results of this study is the lack of correlation of the silicate crystallinity with anything else. This may reflect the diversity in the evolutionary histories of disks (e.g., some make more crystalline silicates than others), which may be a consequence of initial conditions (e.g., initial disk mass and angular momentum) and/or environment (e.g., binarity). Considerable diversity may result from the process of giant planet formation. For example, suppose that within the first 1–3 Myr of existence, all disks accumulate crystalline silicate grains in their inner disks either by inner disk heating and outward radial transport or by local annealing of silicate grains. Suppose further that a giant planet forms in the inner disk. According to Quillen et al. (2004), the planet clears a gap in the disk and absorbs the accretion from the outer disk. The inner disk is cleared by accretion onto the star in $\sim 10^5$ yr, leaving a transitional disk with the characteristics of the disk around either CoKu Tau/4 or DM Tau. The remnant outer disk has very few crystalline silicate dust grains remaining,

also like CoKu Tau/4. If the disk is sufficiently massive, as is the case with DM Tau, the planet can migrate radially inward. If this planet formation and migration scenario happens with sufficient frequency in T Tauri disks, a large number of T Tauri disks with near IR excesses not indicating transitional disks but with $10\ \mu\text{m}$ features indicating low crystallinity, like FM Tau, will be observed. Both giant planet formation and crystallization can depend on the disk/star mass ratio, but crystallized dust can be removed after the planet forms.

In a future paper, the relative abundances of various dust species in a larger sample of T Tauri disks will be quantified, and the abundances of dust species will be compared to other dust species and also to various stellar properties. Another goal is to incorporate the best-fit dust cross-sections for our T Tauri objects into the sophisticated radiative transfer models described by Calvet et al. (1991, 1992), and D’Alessio et al. (1998, 1999, 2001) to model these objects’ SEDs and spectra self-consistently over much wider wavelength ranges.

This work is based on observations made with the *Spitzer Space Telescope*, which is operated by the Jet Propulsion Laboratory, California Institute of Technology under NASA contract 1407. Support for this work was provided by NASA through contract 1257184 issued by JPL/Caltech and through the Spitzer Fellowship Program, under award 011 808-001, and JPL contract 960803 to Cornell University, and Cornell subcontracts 31419-5714 to the University of Rochester. The authors thank Ciska Markwick-Kemper for offering $10\ \mu\text{m}$ data for GCS 3 and for helpful comments on the paper. The authors also acknowledge helpful comments from Luke Keller. P. D. acknowledges grants from PAPIIT, DGAPA, UNAM and CONACyT, México. N. C. and L. H. acknowledge support from NASA grant NAG5-13210, STScI grant AR-09524.01-A, and NASA Origins grant NAG5-9670. A.L. acknowledges support from the University of Missouri Summer Research Fellowship, the University of Missouri Research Board, and the NASA award P20436. SMART was developed by the IRS Team at Cornell University and is available through the *Spitzer* Science Center at Caltech. This publication makes use of the Jena-St. Petersburg Database of Optical Constants (Henning et al. 1999).

Appendix

In our attempts to fit the dust emission feature at $\sim 11.3\ \mu\text{m}$ in many of our emissivities, we unexpectedly found a very close resemblance between the opacity profile of forsterite grains with a CDE shape distribution and that of porous forsterite grains with a volume fraction of vacuum $f = 0.6$ (i.e. 60% of the grain volume is vacuum) and a fractal dimension of $D = 2.766$. For these porous grains, we used the Bruggeman effective medium theory

(Bohren & Huffman 1983) and the dielectric constants of forsterite of Fabian et al. (2001) to generate the effective dielectric constants for each crystalline axis. For a given crystalline axis, we generate opacity from Mie theory using the effective dielectric constants for that axis, assuming a spherical grain radius of $0.1 \mu\text{m}$. We then obtain the opacity for the porous forsterite grain by averaging the opacities of all three crystalline axes. The resulting porous forsterite opacity is nearly identical to that derived using the same set of dielectric constants and assuming a CDE shape distribution (Figure 14). We made the same comparison using parameters for the ordinary and extraordinary rays of α quartz (Wenrich & Christensen 1996). As for forsterite, we used $f = 0.6$, $D = 2.766$, and grain radius of $0.1 \mu\text{m}$; however, for quartz we add the sum of $\frac{2}{3}$ of the opacity generated from the ordinary ray and $\frac{1}{3}$ of that from the extraordinary ray. As for forsterite, the quartz opacities generated assuming porous grains and grains with a CDE distribution are nearly identical (see Figure 14). This suggests that the near-equivalence of the Bruggeman EMT plus Mie theory to CDE is mathematical in nature and not specific to the optical properties of the dust material in question.

REFERENCES

- Adams, F. C., Lada, C. J., & Shu, F. H. 1987, *ApJ*, 312, 788
- Andrews, S. M., & Williams, J. P. 2005, *ApJ*, 631, 1134
- Baraffe, I., Chabrier, G., Allard, F., & Hauschildt, P. H. 1998, *A&A*, 337, 403
- Beckwith, S. V. W., Sargent, A. I., Chini, R. S., & Guesten, R. 1990, *AJ*, 99, 924
- Bohren, C. F., & Huffman, D. R. 1983, *Absorption and Scattering of Light by Small Particles*, New York: Wiley
- Boss, A. P. 2004, *ApJ*, 616, 1265
- Boss, A. P., & Durisen, R. H. 2005a, *ApJ*, 621, L137
- Boss, A. P., & Durisen, R. H. 2005b, *ASP Conf. Ser.* 341: Chondrites and the Protoplanetary Disk, 341, 821
- Bouwman, J., Meeus, G., de Koter, A., Hony, S., Dominik, C., & Waters, L. B. F. M. 2001, *A&A*, 375, 950
- Bradley, J. 2003, *LNP Vol. 609: Astromineralogy*, 609, 217
- Brott, I., & Hauschildt, P. H. 2005, *ESA SP-576: The Three-Dimensional Universe with Gaia*, 565

- Brucato, J. R., Colangeli, L., Mennella, V., Palumbo, P., & Bussoletti, E. 1999, *A&A*, 348, 1012
- Calvet, N., Patino, A., Magris, G. C., & D’Alessio, P. 1991, *ApJ*, 380, 617
- Calvet, N., Magris, G. C., Patino, A., & D’Alessio, P. 1992, *Rev. Mex. de Astro. Astrof.*, 24, 27
- Calvet, N., D’Alessio, P., Hartmann, L., Wilner, D., Walsh, A., & Sitko, M. 2002, *ApJ*, 568, 1008
- Calvet, N., et al. 2005, *ApJ*, 630, L185
- Chihara, H., Koike, C., Tsuchiyama, A., Tachibana, S., & Sakamoto, D. 2002, *A&A*, 391, 267
- Cohen, M. 1973, *MNRAS*, 164, 395
- Cohen, M., & Witteborn, F. C. 1985, *ApJ*, 294, 345
- Cohen, M., Megeath, S. T., Hammersley, P. L., Martín-Luis, F., & Stauffer, J. 2003, *AJ*, 125, 2645
- D’Alessio, P., Canto, J., Calvet, N., & Lizano, S. 1998, *ApJ*, 500, 411
- D’Alessio, P., Calvet, N., Hartmann, L., Lizano, S., & Cantó, J. 1999, *ApJ*, 527, 893
- D’Alessio, P., Calvet, N., & Hartmann, L. 2001, *ApJ*, 553, 321
- D’Alessio, P., et al. 2005, *ApJ*, 621, 461
- D’Alessio, P., et al. 2006, *ApJ*, 638, 314
- Desch, S. J., & Connolly, H. C. 2002, *Meteoritics & Planet. Sci.*, 37, 183
- Dorschner, J., Begemann, B., Henning, T., Jaeger, C., & Mutschke, H. 1995, *A&A*, 300, 503
- Dorschner, J. 2003, *LNP Vol. 609: Astromineralogy*, 609, 1
- Draine, B. T., & Lee, H. M. 1984, *ApJ*, 285, 89
- Draine, B. T. 2003, *ARA&A*, 41, 241
- Dyck, H. M., Capps, R. W., Forrest, W. J., & Gillett, F. C. 1973, *ApJ*, 183, L99
- Etchepare, J., Merian, M., & Kaplan, P. 1978, *J. Chem. Phys.*, 68, 1531

- Fabian, D., Jäger, C., Henning, T., Dorschner, J., & Mutschke, H. 2000, *A&A*, 364, 282
- Fabian, D., Henning, T., Jäger, C., Mutschke, H., Dorschner, J., & Wehrhan, O. 2001, *A&A*, 378, 228
- Forrest, W. J., Houck, J. R., & Reed, R. A. 1976, *ApJ*, 208, L133
- Forrest, W. J., & Soifer, B. T. 1976, *ApJ*, 208, L129
- Forrest, W. J., McCarthy, J. F., & Houck, J. R. 1979, *ApJ*, 233, 611
- Forrest, W. J., et al. 2004, *ApJS*, 154, 443
- Furlan, E., et al. 2005a, *ApJ*, 621, L129
- Furlan, E., et al. 2005b, *ApJ*, 628, L65
- Gail, H.-P. 2004, *A&A*, 413, 571
- Geoffroy, H., & Monin, J.-L. 2001, *A&A*, 369, 239
- Gillett, F. C., Low, F. J., & Stein, W. A. 1968, *ApJ*, 154, 677
- Harker, D. E., & Desch, S. J. 2002, *ApJ*, 565, L109
- Harker, D. E., Wooden, D. H., Woodward, C. E., & Lisse, C. M. 2002, *ApJ*, 580, 579
- Hartmann, L., Calvet, N., Gullbring, E., & D'Alessio, P. 1998, *ApJ*, 495, 385
- Henning, T., Il'In, V. B., Krivova, N. A., Michel, B., & Voshchinnikov, N. V. 1999, *A&AS*, 136, 405
- Herczeg, G. J., Wood, B. E., Linsky, J. L., Valenti, J. A., & Johns-Krull, C. M. 2004, *ApJ*, 607, 369
- Higdon, S. J. U., et al. 2004, *PASP*, 116, 975
- Honda, M., Kataza, H., Okamoto, Y. K., Miyata, T., Yamashita, T., Sako, S., Takubo, S., & Onaka, T. 2003, *ApJ*, 585, L59
- Houck, J. R., et al. 2004, *ApJS*, 154, 18
- Jayawardhana, R., Hartmann, L., Fazio, G., Fisher, R. S., Telesco, C. M., & Piña, R. K. 1999, *ApJ*, 520, L41
- Jones, T. W., & Merrill, K. M. 1976, *ApJ*, 209, 509

- Kemper, F., Vriend, W. J., & Tielens, A. G. G. M. 2004, *ApJ*, 609, 826 (erratum: 633, 534)
- Kenyon, S. J., & Hartmann, L. 1987, *ApJ*, 323, 714
- Kenyon, S. J., & Hartmann, L. 1995, *ApJS*, 101, 117
- Kessler, M. F., et al. 1996, *A&A*, 315, L27
- Kessler-Silacci, J. E., Hillenbrand, L. A., Blake, G. A., & Meyer, M. R. 2005, *ApJ*, 622, 404
- Kessler-Silacci, J., et al. 2006, *ApJ*, 639, 275
- Koike, C., Shibai, H., & Tuchiya, A. 1993, *MNRAS*, 264, 65
- Levesque, E. M., Massey, P., Olsen, K. A. G., Plez, B., Josselin, E., Maeder, A., & Meynet, G. 2005, *ApJ*, 628, 973
- Li, A., & Draine, B. T. 2001, *ApJ*, 550, L213
- Li, A., & Greenberg, J. M. 1997, *A&A*, 323, 566
- Li, A., & Greenberg, J. M. 1998, *ApJ*, 498, L83
- Li, A., & Lunine, J. I. 2003, *ApJ*, 590, 368
- Lisse, C. M., A’Hearn, M. F., Hauser, M. G., Kelsall, T., Lien, D. J., Moseley, S. H., Reach, W. T., & Silverberg, R. F. 1998, *ApJ*, 496, 971
- Mendoza, V. E. E. 1966, *ApJ*, 143, 1010
- Najita, J., Carr, J. S., & Mathieu, R. D. 2003, *ApJ*, 589, 931
- Natta, A., Meyer, M. R., & Beckwith, S. V. W. 2000, *ApJ*, 534, 838
- Pilipp, W., Hartquist, T. W., Morfill, G. E., & Levy, E. H. 1998, *A&A*, 331, 121
- Pollack, J. B., Hollenbach, D., Beckwith, S., Simonelli, D. P., Roush, T., & Fong, W. 1994, *ApJ*, 421, 615
- Przygodda, F., van Boekel, R., Àbrahàm, P., Melnikov, S. Y., Waters, L. B. F. M., & Leinert, C. 2003, *A&A*, 412, L43
- Quillen, A. C., Blackman, E. G., Frank, A., & Varnière, P. 2004, *ApJ*, 612, L137
- Rogers, C., Martin, P. G., & Crabtree, D. R. 1983, *ApJ*, 272, 175

- Rucinski, S. M. 1985, *AJ*, 90, 2321
- Shu, F. H., Shang, H., & Lee, T. 1996, *Science*, 271, 1545
- Siess, L., Dufour, E., & Forestini, M. 2000, *A&A*, 358, 593
- Simon, M., & Prato, L. 1995, *ApJ*, 450, 824
- Sloan, G. C., Kraemer, K. E., Price, S. D., & Shipman, R. F. 2003, *ApJS*, 147, 379
- Sogawa, H., Kozasa, T., Koike, C., & Suto, H. 1999, in *Proceedings of the 32nd ISAS Lunar and Planetary Symposium 32*, ed. H. Mizutani & M. Kato (Sagamihara: Inst. of Space and Aeronautical Science), 175
- Speck, A. K. 1998, Ph.D. Thesis, University College London
- Torres, G., Guenther, E. W., Marschall, L. A., Neuhäuser, R., Latham, D. W., & Stefanik, R. P. 2003, *AJ*, 125, 825
- Uchida, K. I., et al. 2004, *ApJS*, 154, 439
- van Boekel, R., Waters, L. B. F. M., Dominik, C., Bouwman, J., de Koter, A., Dullemond, C. P., & Paresce, F. 2003, *A&A*, 400, L21
- van Boekel, R., et al. 2004, *Nature*, 432, 479
- van Boekel, R., Min, M., Waters, L. B. F. M., de Koter, A., Dominik, C., van den Ancker, M. E., & Bouwman, J. 2005, *A&A*, 437, 189
- Watson, D. M., et al. 2004, *ApJS*, 154, 391
- Watson, D. M., et al. 2006, in preparation
- Webb, R. A., Zuckerman, B., Platais, I., Patience, J., White, R. J., Schwartz, M. J., & McCarthy, C. 1999, *ApJ*, 512, L63
- Weidenschilling, S. J. 1997, *Icarus*, 127, 290
- Weintraub, D. A., Saumon, D., Kastner, J. H., & Forveille, T. 2000, *ApJ*, 530, 867
- Wenrich, M. L., & Christensen, P. R. 1996, *J. Geophys. Res.*, 101, 15921
- Werner, M. W., et al. 2004, *ApJS*, 154, 1
- White, R. J., Ghez, A. M., Reid, I. N., & Schultz, G. 1999, *ApJ*, 520, 811

Wilner, D. J., Ho, P. T. P., Kastner, J. H., & Rodríguez, L. F. 2000, *ApJ*, 534, L101

Wood, J. A. 1996, *Meteoritics & Planet. Sci.*, 31, 641

Zubko, V. G., Mennella, V., Colangeli, L., & Bussoletti, E. 1996, *MNRAS*, 282, 1321

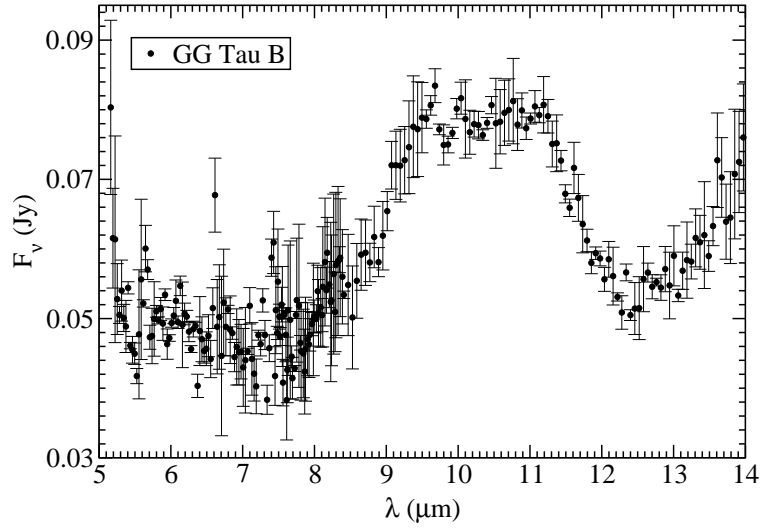


Fig. 1.— The 5–14 μm IRS spectrum of GG Tau B.

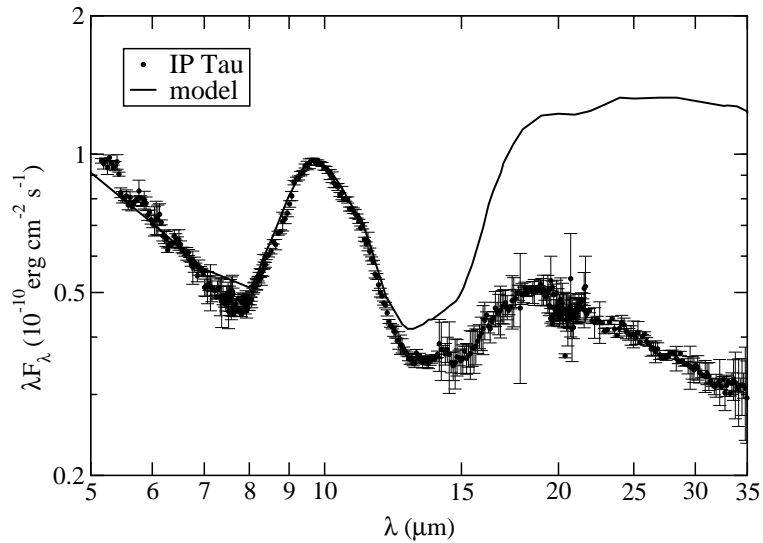


Fig. 2.— The 5–35 μm IRS spectrum of IP Tau fit by a disk model using a dust mixture similar to that from Table 4 for IP Tau.

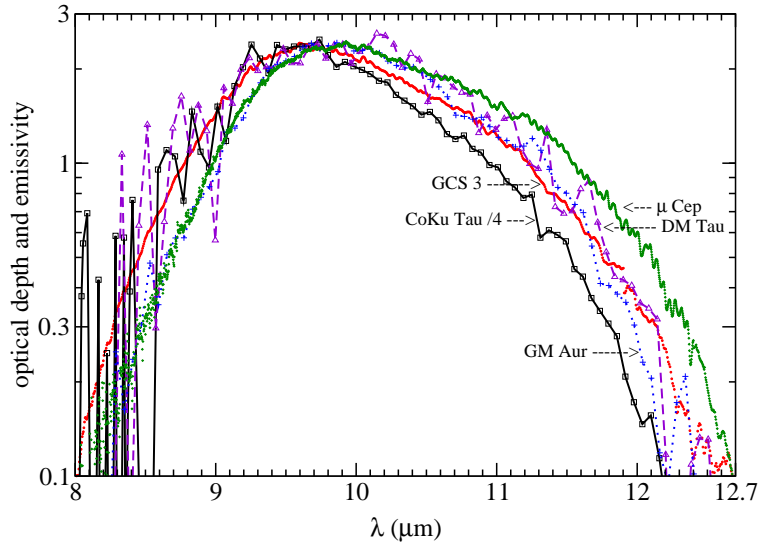


Fig. 3.— The 10 μm silicate profiles of GCS 3, CoKu Tau/4, DM Tau, GM Aur, and μ Cep. The GCS 3 profile of Kemper et al. (2004) is the interstellar silicate absorption toward the Galactic center and the other four profiles are scaled emissivities with baselines subtracted (see Table 3).

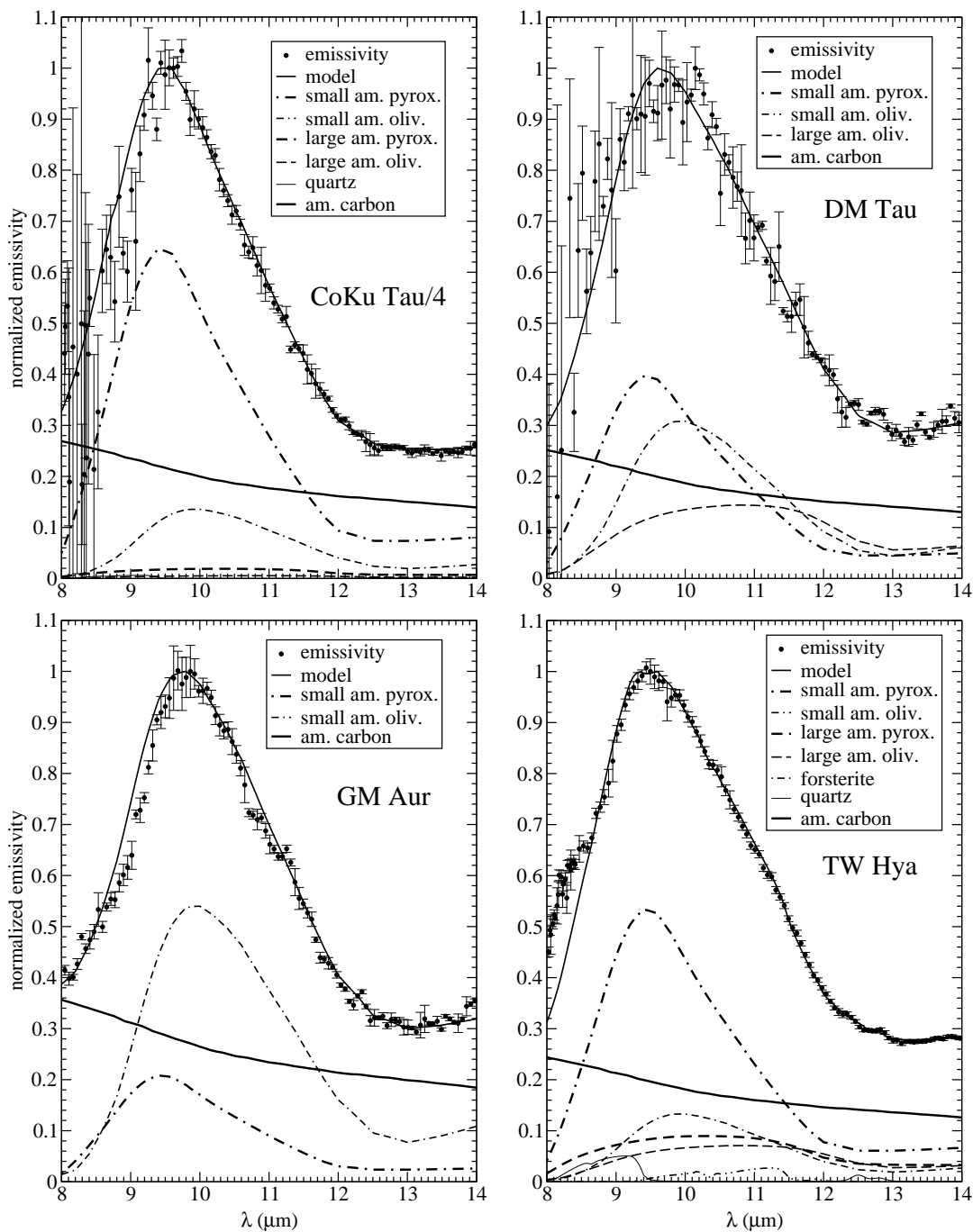


Fig. 4.— Derived emissivities of CoKu Tau/4, DM Tau, GM Aur, and TW Hya. Also displayed are the dust model spectra, as well as the spectrum of each dust component.

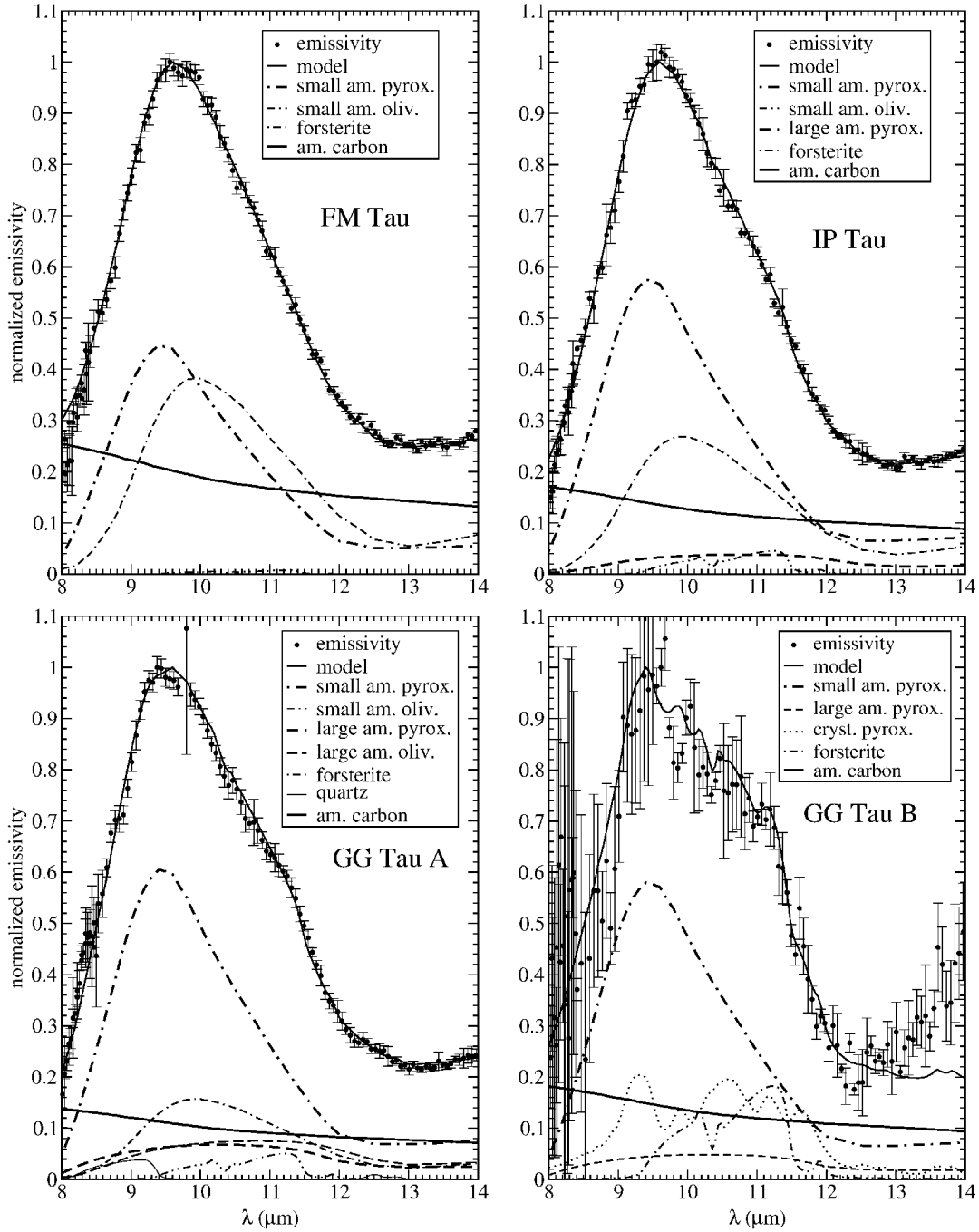


Fig. 5.— Same as Fig. 4, but for FM Tau, IP Tau, GG Tau A, and GG Tau B.

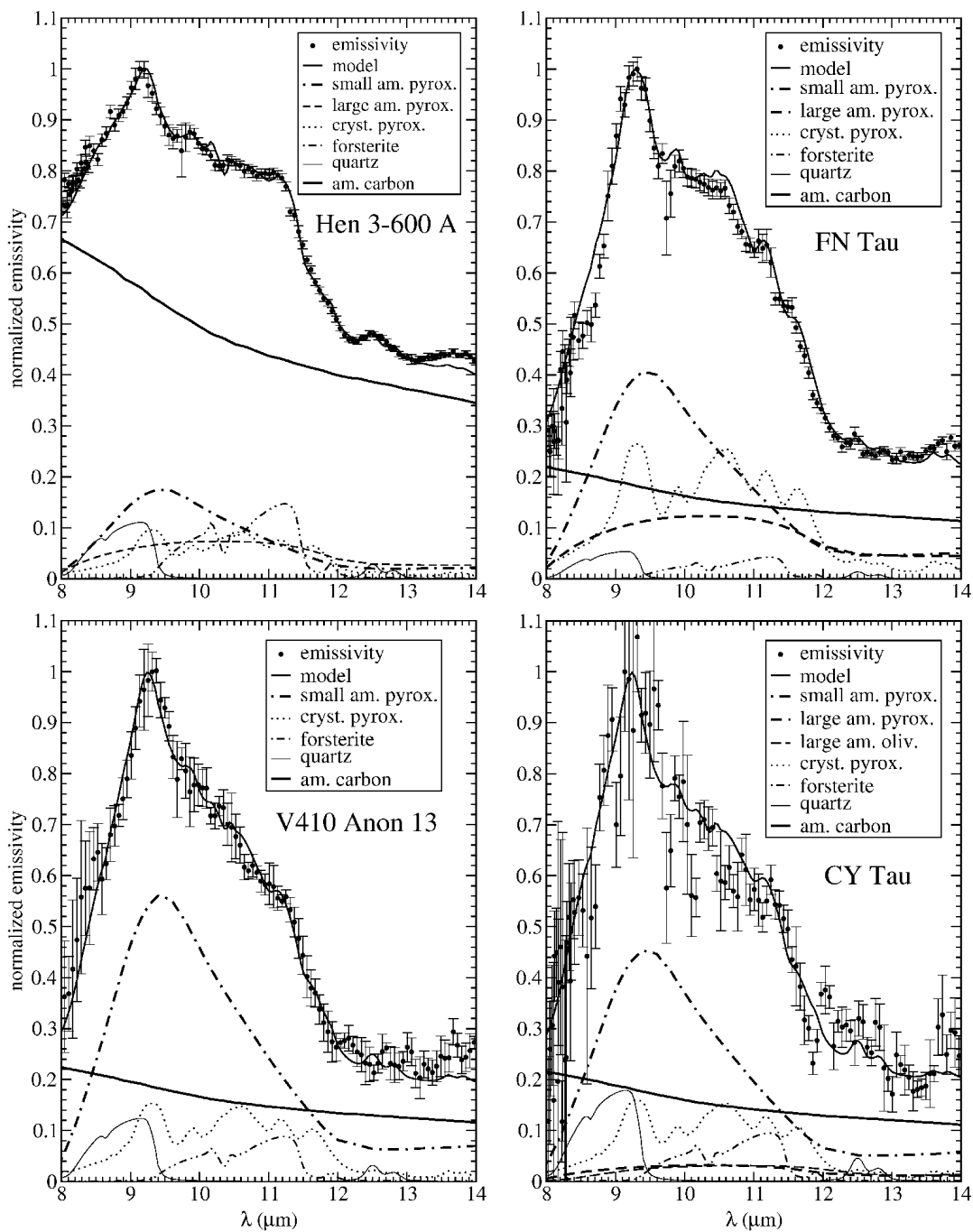


Fig. 6.— Same as Fig. 4, but for Hen 3-600 A, FN Tau, V410 Anon 13, and CY Tau.

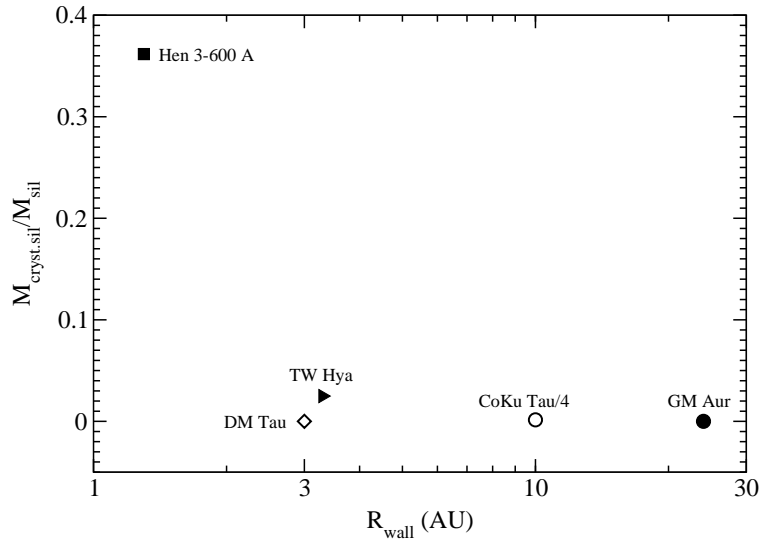


Fig. 7.— Mass fraction of crystalline silicate dust vs. radial location of wall for transitional disks.

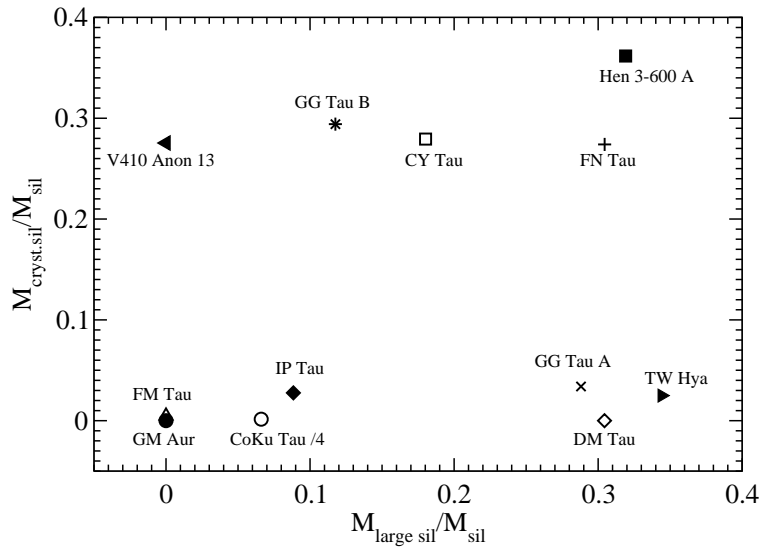


Fig. 8.— Mass fraction of crystalline silicates vs. that of large silicate grains for all 12 Tauri stars.

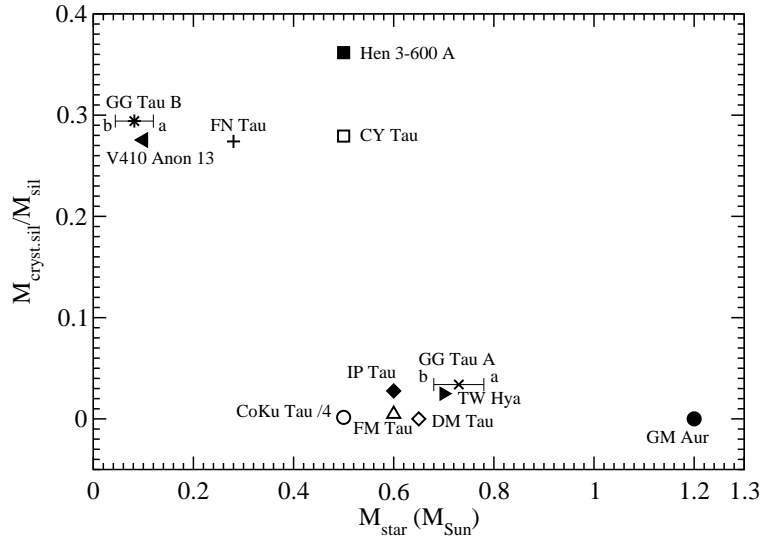


Fig. 9.— Mass fraction of crystalline silicate grains vs. stellar mass for all 12 T Tauri stars. The stellar mass plotted for Hen 3-600 A (a spectroscopic binary) is the sum of the masses of its two components.

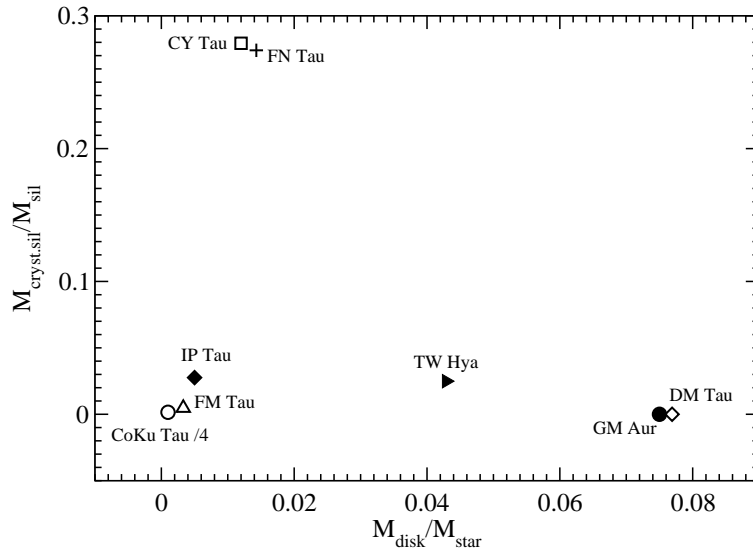


Fig. 10.— Mass fraction of crystalline silicate dust vs. disk-to-star mass ratio.

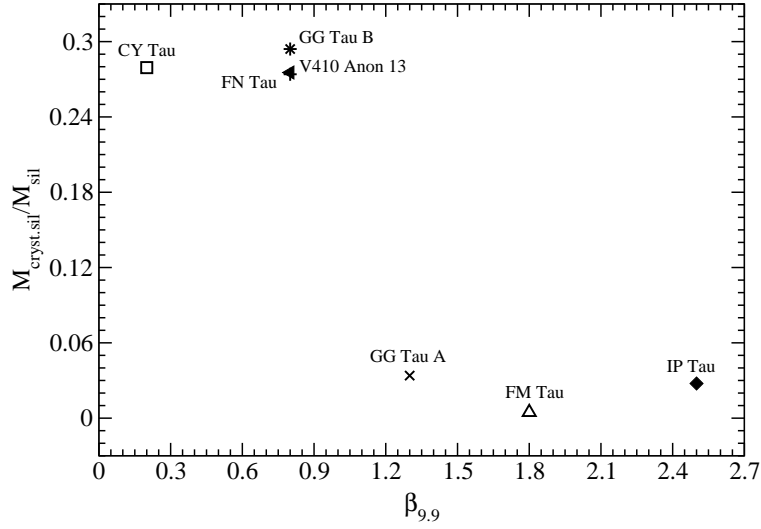


Fig. 11.— Mass fraction of crystalline silicate dust vs. $\beta_{9.9}$ – the continuum-subtracted residual flux at 9.9 μm to the 9.9 μm continuum for “full disks”.

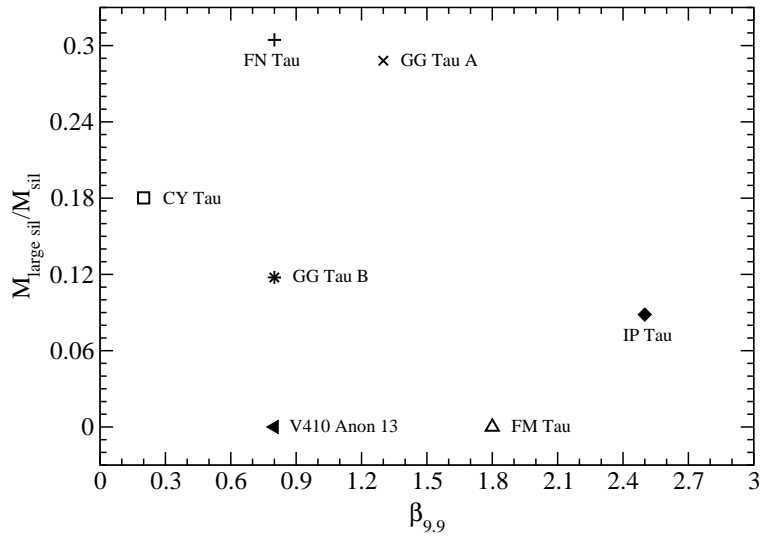


Fig. 12.— Mass fraction of large silicate grains vs. $\beta_{9.9}$ for “full disks.”

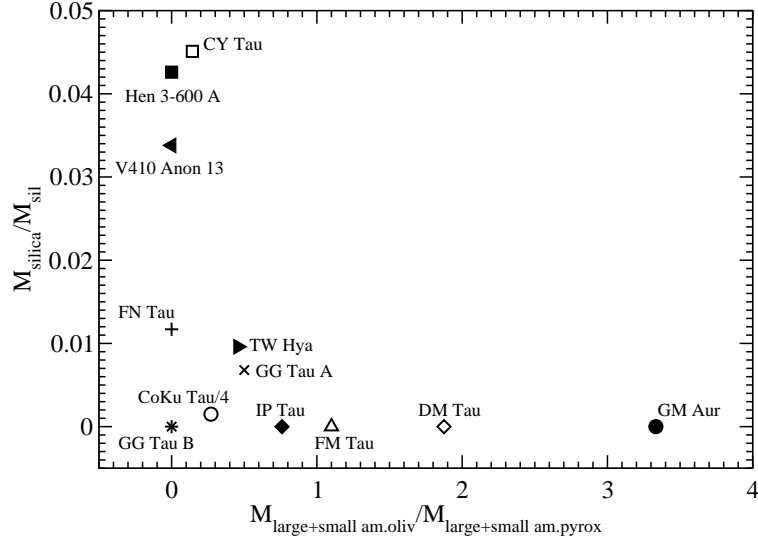


Fig. 13.— Mass fraction of quartz vs. mass ratio of amorphous olivine to amorphous pyroxene for all 12 T Tauri stars.

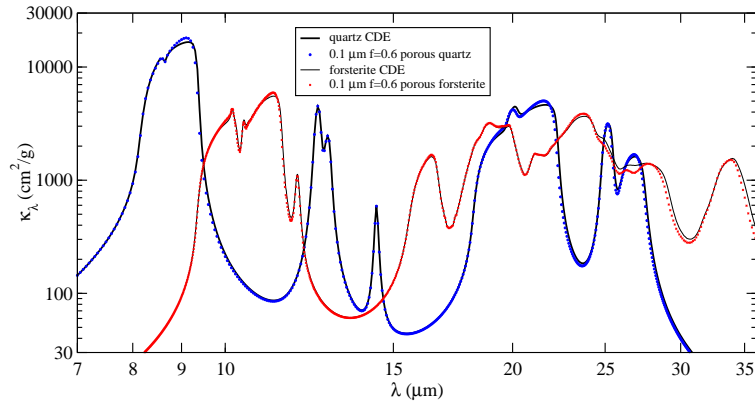


Fig. 14.— Comparison of opacity profile of solid α quartz (*thick line*) and forsterite (*thin line*) with a CDE shape distribution with that for porous α quartz (*blue circles*) and forsterite (*red circles*).

Table 1. The T Tauri Sample

Object	Spectral Type	A_V (mag)	T_{eff} (K)	L_* (L_\odot)	M_* (M_\odot)	M_{disk} ($10^{-3} M_\odot$)	M_{disk}/M_*
CoKu Tau/4	M1.5 ^a	3.0 ^a	3720 ^a	0.61 ^a	0.5 ^j	0.5 ^k	0.001
DM Tau	M1 ^b	0.5 ^b	3720 ^b	0.25	0.65 ^b	50 ^b	0.077
GM Aur	K5 ^b	1.2 ^b	4730 ^b	0.83	1.2 ^b	90 ^b	0.075
TW Hya	K7 ^c	0 ^d	4009 ^c	0.25 ^c	0.7 ^j	30 ^e	0.043
FM Tau	M0	0.69	3850	0.32	0.6 ^j	2 ^k	0.003
IP Tau	M0	0.24	3850	0.43	0.6 ^j	3 ^k	0.005
GG Tau Aa	K7 ^f	0.8 ^f	4060 ^g	0.84 ^f	0.78 ^f
GG Tau Ab	M0.5 ^f	3.2 ^f	3850 ^g	0.71 ^f	0.68 ^f
GG Tau Ba	M5 ^f	0.55 ^f	3050 ^f	0.08 ^f	0.12 ^f
GG Tau Bb	M7 ^f	0 ^f	2820 ^f	0.02 ^f	0.044 ^f
Hen 3-600 A	M3e ^c	0.7 ⁱ	3350 ^c	0.2 ^c	0.5 ^j
FN Tau	M5	1.35	3240	0.5	0.28 ^j	4 ^l	0.014
V410 Anon 13	M5.75 ^h	5.8 ^h	3000 ^h	0.077 ^h	0.1 ^h
CY Tau	M1	0.1	3720	0.47	0.5 ^j	6 ^k	0.012

Note. — For Hen 3-600 A, we determine the mass for each of the two components of the spectroscopic binary, assuming that (1) both components have the same luminosity, (2) the two components’ combined luminosity is the same as that plotted in Figure 3 of Webb et al. (1999) for Hen 3-600 A, and (3) the effective temperatures of both components are the same and equal to that plotted for Hen 3-600 A in Figure 3 of Webb et al. (1999). We then derive mass for one of the components from Siess et al. (2000), and add the masses (to plot a point for Hen 3-600 A in Figure 7 and Table 1).

Note. — All data from Kenyon & Hartmann (1995) unless otherwise noted.

^afrom D’Alessio et al. (2005)

^bfrom Calvet et al. (2005)

^cfrom Webb et al. (1999)

^dfrom Herczeg et al. (2004)

^efrom Wilner et al. (2000)

^ffrom White et al. (1999)

^g T_{eff} from Kenyon & Hartmann (1995) based on the spectral type of White et al. (1999)

^hfrom Furlan et al. (2005a)

ⁱfrom Geoffroy & Monin (2001)

^jusing Siess et al. (2000)

^kfrom Andrews & Williams (2005)

^lfrom Beckwith et al. (1990)

Table 2: Emissivity Modeling Parameters

Object ^a	Ω_* (10^{-19} sr)	T_* (K)	F_{10} (Jy)	power index m	λ_s (μm)	λ_l (μm)	ϵ_l/ϵ_s	T_d (K)	$\Omega_d\tau_{max}$ (10^{-16} sr)	$\beta_{9.9}^b$
μ Cep	43300	3500	10.0	18.2	0.64	423	12650	5.1
CoKu Tau/4	2.6	3720	10.0	20.0	0.50	121	1227	*
DM Tau	1.2	3720	9.5	19.0	0.59	160	89.4	*
GM Aur	1.5	4730	9.4	18.8	0.58	310	6.1	*
TW Hya	7.9	4009	9.65	19.3	0.56	193	293.8	*
FM Tau	0.131	-0.388	10.0	20.0	0.50	222	41.4	1.8
IP Tau	0.090	-0.936	10.0	20.0	0.52	259	15.5	2.5
GG Tau A	0.445	-0.456	9.65	19.3	0.56	252	49.8	1.3
GG Tau B	0.042	-0.370	10.0	20.0	0.67	252	3.3	0.8
Hen 3-600 A	19.3	3350	9.65	19.3	0.65	229	126.0	*
FN Tau	0.339	0.161	10.0	20.0	0.71	208	86.1	0.8
V410 Anon 13	0.017	-0.433	10.0	20.0	0.63	256	1.3	0.8
CY Tau	0.120	-0.627	10.0	20.0	0.69	239	3.7	0.2

^aFor the transitional disk sources (CoKu Tau/4, DM Tau, GM Aur, TW Hya, Hen 3-600 A), we subtract $\Omega_* B_\nu(T_*)$, representing the photospheric emission, from the dereddened IRS spectra to isolate the optically thin emission in the $10 \mu\text{m}$ complex; for other sources, a power law is fit to the $\lambda < 8 \mu\text{m}$ IRS spectrum and subtracted. The power law is represented by $F_\nu(\lambda) = F_{10} (\lambda/10 \mu\text{m})^m$, where F_{10} is the flux density at $10 \mu\text{m}$ in Janskys. To determine the dust temperature T_d , the excess flux and the model opacity are determined at wavelength regions centered at λ_{short} and λ_{long} . Dividing these blackbody- or continuum-subtracted residuals by a Planck function of T_d , gives the relative emissivities. These emissivities are divided by the normalization constant $\Omega_d\tau_{max}$, where τ_{max} is the maximum optical depth in the $10 \mu\text{m}$ feature of the optically thin residual flux.

^b $\beta_{9.9}$ is the ratio of the continuum-subtracted residual at $\sim 9.9 \mu\text{m}$ to the $\sim 9.9 \mu\text{m}$ continuum (which was subtracted to derive the residuals). The asterisks (*) for CoKu Tau/4, DM Tau, GM Aur, TW Hya, and Hen 3-600 A indicate that there is no detectable disk flux continuum underneath their $10 \mu\text{m}$ feature, so their $\beta_{9.9}$ are effectively infinity. For μ Cep, the continuum is the stellar blackbody.

Table 3. Parameters for Silicate Profiles

Object	ϵ_8	ϵ_{13}	scaling factor
μ Cep	0.21	0.44	3.4
CoKu Tau /4	0.33	0.25	3.4
DM Tau	0.53	0.29	4.5
GM Aur	0.42	0.30	3.9

Note. — The $10\ \mu\text{m}$ profiles plotted in Figure 4 were derived by subtracting a linear baseline from the emissivities of CoKu Tau/4, DM Tau, and GM Aur from Figure 4 and μ Cep (not shown here), and scaling the residuals to the peak value of the optical depth of GCS 3. The second and third columns give the values of the emissivity baseline at ~ 8 and $\sim 13\ \mu\text{m}$, respectively. After subtracting the baseline, the residual emissivity was multiplied by the fourth column.

Table 4: Dust Mass Percentages and Reduced χ^2

Object	small am. pyrox ^a	small am. oliv ^b	large am. pyrox ^c	large am. oliv ^d	am. carbon ^e	cryst. pyrox ^f	cryst. forst ^g	cryst. quartz ^h	$\frac{\chi^2}{\text{d.o.f.}}$ ⁱ	cryst. silicates ^j	large silicates ^h
μ Cep	0	100	0	0	0	0	0	0	...	0	0
CoKu Tau/4	47.8	12.9	3.3	1.0	34.9	0	0	0.1	2.3	0.15	6.6
DM Tau	25.1	25.1	0	21.9	27.9	0	0	0	6.6	0	30.4
GM Aur	13.6	45.5	0	0	40.9	0	0	0	9.8	0	0
TW Hya	34.6	11.1	13.8	11.1	27.7	0	1.1	0.7	31.1	2.5	34.4
FM Tau	32.2	35.4	0	0	32.2	0	0.3	0	2.0	0.47	0
IP Tau	42.9	25.8	0	6.9	22.3	0	2.1	0	3.0	2.8	8.8
GG Tau A	42.3	14.1	11.3	12.7	16.9	0	2.3	0.6	1.7	3.4	28.8
GG Tau B	44.4	0	8.9	0	24.4	13.3	8.9	0	2.5	29.4	11.8
Hen 3-600 A	10.2	0	10.2	0	68.0	4.8	5.4	1.4	4.8	36.2	31.9
FN Tau	30.2	0	21.8	0	28.5	16.8	2.0	0.8	4.0	27.4	30.4
V410 Anon 13	48.1	0	0	0	33.7	11.2	4.8	2.2	1.9	27.5	0
CY Tau	37.3	0	6.2	6.2	31.1	11.2	5.0	3.1	2.3	27.9	18.0

^aOptical constants for amorphous pyroxene $\text{Mg}_{0.8}\text{Fe}_{0.2}\text{SiO}_3$ from Dorschner et al. (1995), assuming CDE2 (Fabian et al. 2001)

^bOptical constants for amorphous olivine MgFeSiO_4 from Dorschner et al. (1995), assuming CDE2

^cOptical constants for amorphous pyroxene $\text{Mg}_{0.8}\text{Fe}_{0.2}\text{SiO}_3$ from Dorschner et al. (1995), using the Bruggeman EMT and Mie theory (Bohren & Huffman 1983) with a volume fraction of vacuum of $f = 0.6$ for porous spherical grains of radius $5 \mu\text{m}$

^dOptical constants for amorphous olivine MgFeSiO_4 from Dorschner et al. (1995), using the Bruggeman EMT and Mie theory (Bohren & Huffman 1983) with a volume fraction of vacuum of $f = 0.6$ for porous spherical grains of radius $5 \mu\text{m}$

^eOptical constants for amorphous carbon (“ACAR”) from Zubko et al. (1996), assuming CDE2

^fOpacities for crystalline pyroxene $\text{Mg}_{0.9}\text{Fe}_{0.1}\text{SiO}_3$ from Chihara et al. (2002)

^gOptical constants for 3 crystallographic axes of forsterite, $\text{Mg}_{1.9}\text{Fe}_{0.1}\text{SiO}_4$, from Fabian et al. (2001), assuming CDE (Bohren & Huffman 1983)

^hOptical properties for α quartz from Wenrich & Christensen (1996), assuming CDE

ⁱ χ^2/dof (dof=8) is determined over $8 < \lambda < 14 \mu\text{m}$

^jPercentage of crystalline dust (pyroxene, forsterite and silica) compared to all silicates in the dust model.

^hPercentage of large silicate dust (large amorphous pyroxene and large amorphous olivine) compared to all silicates in the dust model.